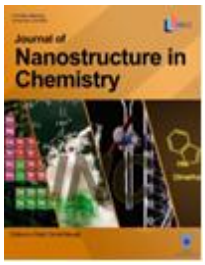

Volume 16, Issue 3, 2026: 212-237

Journal of Nanostructure in Chemistry (JNSC)

https://doi.org/10.57647/jnsc.2026.1603.11

Research Article

Design of a Calcium-Triggered Nanostructured Delivery System for Controlled In Vitro Release of Trypsin Inhibitor

Yugang Qin[1], Wenxuan Zhang[1], Bolun Zhang[1], Gaoxue Li[2], Yongbiao Ma[3], Qiang Zhang[1], Xiaojun Wei[1], Yang Xu[1*]

[1] *Department of Hepatobiliary Surgery, Aerospace Center Hospital, Beijing, 100049, China*
[2] *Department of Gastroenterology, Shouguang People's Hospital, Shouguang, Shandong, 262702, China*
[3] *Department of Pancreatic Surgery Weifang People's Hospital, Weifang, Shandong, 261100, China*

***Corresponding authors:** htzy721gdwk@163.com ; 59971387@asch.net.cn

Article History:

Received:
11 December 2025

Revised:
07 January 2026

Accepted:
03 February 2026

Published in Issue:
30 June 2026

Abstract

We report a mesoporous silica nanoparticle platform that exploits physiological divalent ions as a benign trigger to control stage-specific protein release under gastrointestinal-mimicking in vitro conditions, using soybean trypsin inhibitor as a model cargo. Spherical pore-expanded MSNs (~300 nm, pore diameter ~3.8 nm, BET surface area ~800 m^2/g) were synthesized, loaded with up to 15.6 wt% inhibitor at 75% encapsulation efficiency, and then capped with an ~8 wt% PVA–borate nanogel gate to yield PB-MSN composites containing 14.5 wt% protein. Structural, textural and dispersion analyses confirmed that the coating partially occluded pore mouths while preserving the mesoporous framework and improving colloidal stability. In a two-stage simulated gastrointestinal protocol, PB-MSNs leaked only 3.8 ± 0.5% cargo after 2 h in pH 1.2 medium, whereas uncoated MSNs released 68 ± 5% under the same conditions. Subsequent exposure to pH 7.4 buffer containing 10 mM $CaCl_2$ triggered a rapid burst, with cumulative release reaching ~40% within 0.5 h, 78 ± 3% at 4 h and 88 ± 4% at 8 h; in Ca^2+-free buffer, release remained ≤12.3 ± 1.5% over 8 h, demonstrating a sharp ion-dependent on/off effect. Trypsin activity assays showed that inhibitor liberated under triggering conditions suppressed trypsin activity to a level comparable to free inhibitor, while SGF supernatants exhibited negligible inhibition, indicating substantial retention of inhibitory function in a reductionist activity assay and minimal gastric-phase leakage. The combined data establish PVA–borate-gated MSNs as a modular, ion-responsive platform that decouples protection in acid from fast deployment in near-neutral media. While calcium-responsive carriers and borate-based dynamic networks are well established in other delivery and hydrogel contexts, the present work translates this chemistry into an MSN pore-gating architecture in which Ca^{2+} acts as a competitive borate-binding trigger to dismantle a nanoscale sacrificial gate and thereby generate a sharp 'off/on' release response under GI-mimicking conditions.

Keywords: Mesoporous silica nanoparticles, PVA–borate gate, Gastrointestinal targeting, Protein nanocarriers, Ion-responsive drug platform

Cite this article: Qin Y., Zhang, W., Zhang, B., Li, G., Ma, Y., Zhang, Q., Wei, X., & Xu, Y. (2026). Design of a Calcium-Triggered Nanostructured Delivery System for Controlled In Vitro Release of Trypsin Inhibitor. *J Nanostruct Chem*, **16**, 212-237. https://doi.org/10.57647/jnsc.2026.1603.11

1. Introduction

The development of nanoparticle-based delivery systems has revolutionized controlled drug release, enabling precise spatiotemporal delivery of therapeutics [1]. Mesoporous silica nanoparticles (MSNs) in particular have emerged as versatile carriers due to their high surface area, tunable pore structure, and amenability to surface functionalization [2]. These properties allow MSNs to protect sensitive payloads and modulate release kinetics, addressing challenges such as low bioavailability and off-target effects of many drugs. Stimuli-responsive nanocarriers enable controlled release when a defined physiological or externally applied signal is encountered. In oral delivery, the dominant triggers are pH transitions (enteric dissolution) and enzyme-dependent cleavage. However, both triggers are intrinsically coupled to high inter- and intra-individual variability in the gastrointestinal environment. Gastric pH differs markedly between fasted and fed states, and intestinal pH rises progressively along the small intestine, such that polymer dissolution thresholds (for example, pH-targeted enteric coatings releasing above pH ~6 or ~7) may be exceeded earlier or later depending on physiology and meal conditions [3]. Enzyme-triggered oral systems, especially microbiota-activated designs for distal gut targeting, can also vary with microbiome composition and enzymatic activity [4]. These realities motivated us to explore a complementary, orthogonal trigger: Ca^{2+}, a benign inorganic ion that can be present postprandially and can also be co-administered to standardize the trigger input. Here, we introduce a Ca^{2+}-triggered mesoporous silica nanoparticle system in which release is switched 'on' by Ca^{2+} at constant intestinal pH, enabling quantitative separation of pH-driven effects from ion-triggered gate disassembly.

Delivering therapeutic biomolecules orally poses significant challenges due to the gastrointestinal (GI) tract's harsh conditions. Protein and peptide drugs are vulnerable to degradation by acidic pH in the stomach and proteolytic enzymes in the intestine [5]. As a result, most protein therapeutics (e.g. insulin) must be injected, which reduces patient compliance [6]. To overcome these barriers, advanced oral delivery strategies are being pursued, including protective nanocarriers and co-formulation with enzyme inhibitors [7]. Protease inhibitors can deactivate digestive enzymes and thereby safeguard co-delivered protein drugs from premature breakdown [8]. Indeed, studies have shown that adding trypsin inhibitors like aprotinin or soybean trypsin inhibitor (STI) can significantly improve the intestinal absorption of protein therapeutics [9]. Soybean trypsin inhibitor is a well-known 21 kDa protein (pI ≈4.5) that forms a tight complex with trypsin, blocking its proteolytic activity [10]. Clinically, protease inhibitors have been used as adjuvants for oral delivery platforms [11], although chronic use may induce feedback upregulation of digestive enzymes [12]. Here, we select trypsin inhibitor as an active cargo and model macromolecule, both for its potential role in oral formulations (to neutralize pancreatic trypsin and protect co-delivered drugs) and as a representative protein therapeutic. Prior studies have employed trypsin inhibitors in delivery research [13] – for example, Bhattacharyya et al. [14] used STI as a model to demonstrate sustained release from polymer-coated MSNs. Additionally, STI has been explored as a biopesticide in crop protection, where its controlled release in insect midgut (pH >8) improved efficacy [15]. Building on these insights, a system that releases trypsin inhibitor in response to a specific GI trigger could greatly enhance oral delivery of protein drugs by combining protective and controlled release functions [16, 17].

Calcium ions present an intriguing physiological trigger for drug release. Calcium is abundant in the GI tract (e.g. dietary Ca^{2+} in the small intestine) and plays roles in various biological processes [18]. We hypothesized that a calcium-responsive nanocarrier could remain inert in the stomach (where free Ca^{2+} is low) and then rapidly deploy its cargo upon encountering higher Ca^{2+} levels in the intestine. Previous work has demonstrated calcium-responsive mechanisms in other delivery contexts [19]. For instance, Lou and Best designed liposomes that release contents upon sensing elevated Ca^{2+} associated with certain disease sites [20]. Calcium-triggered release is attractive because Ca^{2+} is a benign stimulus that could be externally administered or endogenously present, allowing non-invasive activation of the delivery system [21]. Despite this potential, few inorganic nanocarriers have leveraged Ca^{2+} as a trigger. One related strategy has been to dope Ca^{2+} into silica networks to create acid-degradable bonds [22]; in tumor microenvironments, such Ca-doped MSNs release Ca^{2+} and drugs under acidic conditions [23][22]. However, for oral delivery, we require stability in acid (stomach) and release in near-neutral conditions (intestine) [24]. To achieve this inverse trigger profile, we introduce a nanostructured MSN system gated by a calcium-sensitive molecular network. Specifically, we coat trypsin inhibitor-loaded MSNs with a thin film of polyvinyl alcohol (PVA) crosslinked by borate ions [25]. This PVA-borate "nanogel" acts as a molecular gate capping the nanopores [26]. In the absence of Ca^{2+}, the borate crosslinks maintain the PVA network, sealing the pores and preventing payload leakage [27]. When Ca^{2+} is present, we hypothesize a competitive interaction in

10.57647/jnsc.2026.1603.11

which Ca^{2+} associates with borate species and shifts borate availability away from diol-bound crosslinks, thereby weakening the borate–diol network and promoting coating permeabilization/disintegration. This hypothesis is chemically plausible given established borate–diol crosslinking in PVA networks and reported Ca^{2+}–borate association/ion-pairing in electrolyte media [28]. We therefore postulate that Ca^{2+} exposure results in dissolution or significant pore opening of the coating, triggering a burst release of the trypsin inhibitor cargo; in this work, this mechanistic picture is supported by converging release, spectroscopic, and post-trigger compositional readouts, while the bond-rupture step itself is not directly measured. Calcium-responsive release strategies have been established in multiple delivery formats, including liposomal systems engineered to respond to elevated Ca^{2+}, and Ca^{2+}-mediated network formation is a classical principle in ionotropic hydrogels [29]. Likewise, borate–diol and related boron-based dynamic crosslinking chemistries are well developed in polymer/hydrogel materials and have been broadly explored as reversible biomedical networks. In this context, the contribution of the present study is not the general concept of Ca^{2+}- or borate-responsive materials, but rather the implementation of a borate-crosslinked PVA nanogel as a nanoscale pore gate on MSNs, where Ca^{2+}–borate association/competition is exploited to dismantle (rather than form) the crosslinked network and thereby generate an inverse GI-relevant trigger profile (acid/low Ca^{2+} 'off' and near-neutral/high Ca^{2+} 'on') [30]. The design takes inspiration from ionotropic gel chemistry (e.g. alginate gels crosslinked by Ca^{2+} [31]), but here the introduction of Ca^{2+} disrupts rather than creates crosslinks – an inverse strategy to achieve on-command disassembly of the gate [32].

In this paper, we report the design, synthesis, and thorough characterization of the proposed calcium-triggered MSN delivery system for controlled in vitro release of trypsin inhibitor. We fabricated spherical mesoporous silica nanoparticles (~300 nm) with expanded ~4 nm pores to accommodate the protein inhibitor. The MSNs were loaded with trypsin inhibitor and then coated with the PVA-borate calcium-responsive gate. We also characterized the loading capacity and conducted in vitro release studies under simulated gastric and intestinal conditions to demonstrate the calcium-triggered release profile. Comparative experiments were performed on ungated MSNs and on control conditions (absence of Ca^{2+}, different pH) to confirm that the release is indeed specifically triggered by Ca^{2+}. Furthermore, the bioactivity of the released inhibitor was verified via trypsin activity assays, illustrating that the inhibitor remains functional after encapsulation and release. The results show that our calcium-triggered nanostructured system achieves minimal release in acidic (Ca^{2+}-free) conditions and a rapid, controlled release when exposed to calcium, effectively fulfilling the design criteria for GI-targeted delivery. This platform provides a mechanistically defined Ca^{2+}-responsive pore-gating architecture for GI-stage-specific release in vitro and, more broadly, for ion-responsive nanocarrier designs. While these results support feasibility for intestinal-stage deployment, demonstration of oral-delivery performance in physiologically complete settings will require standardized multi-component digestion models and in vivo validation, which are beyond the scope of this materials-focused study. In the following sections, we detail the synthesis and characterization of the materials, present the release performance data, and discuss the mechanism and potential applications of this calcium-triggered MSN system in the context of current nanochemical drug delivery research.In this paper, we report the design, synthesis, and thorough characterization of the proposed calcium-triggered MSN delivery system for controlled in vitro release of trypsin inhibitor. We fabricated spherical mesoporous silica nanoparticles (~300 nm) with expanded ~4 nm pores to accommodate the protein inhibitor. The MSNs were loaded with trypsin inhibitor and then coated with the PVA-borate calcium-responsive gate. We also characterized the loading capacity and conducted in vitro release studies under simulated gastric and intestinal conditions to demonstrate the calcium-triggered release profile. Comparative experiments were performed on ungated MSNs and on control conditions (absence of Ca^{2+}, different pH) to confirm that the release is indeed specifically triggered by Ca^{2+}. Furthermore, the bioactivity of the released inhibitor was verified via trypsin activity assays, illustrating that the inhibitor remains functional after encapsulation and release. The results show that our calcium-triggered nanostructured system achieves minimal release in acidic (Ca^{2+}-free) conditions and a rapid, controlled release when exposed to calcium, effectively fulfilling the design criteria for GI-targeted delivery. This platform provides a mechanistically defined Ca^{2+}-responsive pore-gating architecture for GI-stage-specific release in vitro and, more broadly, for ion-responsive nanocarrier designs. While these results support feasibility for intestinal-stage deployment, demonstration of oral-delivery performance in physiologically complete settings will require standardized multi-component digestion models and in vivo validation, which are beyond the scope of this materials-focused study. In the following sections, we detail the synthesis and characterization of the materials, present the release performance data, and

10.57647/jnsc.2026.1603.11

discuss the mechanism and potential applications of this calcium-triggered MSN system in the context of current nanochemical drug delivery research.

2. Materials and Methods

Mesoporous silica nanoparticles (MSNs) were synthesized via a surfactant-templated sol–gel method adapted from the literature [33]. In a typical procedure, the structure-directing agent cetyltrimethylammonium bromide (CTAB) (1.0 g) was dissolved in 480 mL of deionized water, and the solution was brought to ~75 °C under stirring. Sodium hydroxide was added to adjust the pH to ~12.0, facilitating silica condensation [14]. Next, tetraethyl orthosilicate (TEOS) was added dropwise (molar ratio TEOS:CTAB ≈ 1:0.12) and allowed to hydrolyze and condense for 2 h at 75 °C. This yielded a white precipitate of CTAB-templated silica. To introduce porosity suitable for large biomolecules, a pore expansion step was conducted [34]: the as-synthesized silica was transferred to a Teflon-lined autoclave containing a swelling agent (dimethylhexadecylamine, 0.5 g) in 30 mL water and heated at 110 °C for 72 h. This hydrothermal treatment enlarges the template micelles and pore size [35]. The product was filtered, washed with water, and dried under vacuum. Finally, the organic template was removed by solvent extraction to preserve surface functionality (as opposed to calcination which could collapse organics) [36]. The dried silica powder was refluxed in ethanol acidified with 1 M HCl for 48 h to extract CTAB, then washed with ethanol and water. The resulting mesoporous silica nanoparticles were collected and dried (80 °C, 12 h). By this procedure, we obtained MSNs as a white powder. The particles were uniform and white, indicating successful removal of the brownish surfactant residues. Optional Functionalization: In some batches, we introduced surface carboxyl groups by co-condensing 3-triethoxysilyl propyl succinic anhydride (1 mL, added with TEOS) following Bhattacharyya et al. [14]. This carboxylation was intended to facilitate polymer attachment and improve hydrophilicity. Carboxyl-functionalized MSNs were labeled as MSN–COOH. Non-functionalized MSNs were also prepared for comparison by the same method without the silane co-precursor.

The model drug/cargo used in this study is soybean trypsin inhibitor (STI), a 21 kDa protein. Prior to loading, STI was purified and dialyzed into 0.1 M acetic acid (pH ~3) to ensure it was fully protonated and positively charged (note: STI's isoelectric point is ~4.5 [37], so at pH 3 it carries a net positive charge). This promotes electrostatic attraction to the silica pores (negatively charged silanols or carboxylates are deprotonated at neutral pH, but at pH 3 many silanols are protonated; however, some adsorption occurs via hydrogen bonding and confinement effects). MSN samples (typically 200 mg) were dispersed in 10 mL of STI solution (2 mg/mL in 0.1 M acetic acid) and gently shaken for 24 h at room temperature to allow the inhibitor to diffuse into the pores. After loading, the particles were separated by centrifugation (10,000 g, 10 min) and washed lightly with pH 5.0 acetate buffer to remove surface-adhered (but not pore-encapsulated) protein. The amount of trypsin inhibitor loaded was determined by measuring the STI concentration in the supernatant before and after loading, using UV–Vis absorbance at 280 nm (and confirmed by Bradford protein assay). Loading capacity (wt% of STI in the MSN composite) and encapsulation efficiency (fraction of initial STI that was encapsulated) were calculated. We achieved a high loading capacity of ~15 wt% with the pore-expanded MSNs, significantly greater than ~9–10 wt% obtained in non-expanded MSNs. This is consistent with literature reports that larger pore volume improves loading of macromolecules [38]. The carboxyl-functionalized MSNs showed slightly higher loading (by ~2–3%) than non-functionalized, likely due to improved protein-surface interactions, similar to observations by Carneiro et al. [4] who reported ~28% higher adsorption of STI on amino-functionalized silica.

To impart calcium-responsive controlled release, the STI-loaded MSNs were coated with a thin PVA–borate hydrogel that serves as a gatekeeper. Poly(vinyl alcohol) (PVA, 30,000 Da, 98% hydrolyzed) was selected as a biocompatible polymer that can form reversible crosslinks with borate ions (borax) [39][40]. Borate di-esters with PVA's vicinal diols are dynamic and can be disrupted by competitive binding of polyols or certain cations [41]. We exploited this chemistry to create a coating stable in the absence of Ca^{2+} but destabilized when Ca^{2+} is introduced. To coat the particles, STI-loaded MSNs (100 mg) were dispersed in 10 mL of an aqueous solution of PVA (5 wt%) and sodium tetraborate decahydrate (borax, 1 wt%). The mixture was stirred at room temperature for 2 h, during which borate ions crosslinked PVA chains, promoting deposition of a nanogel layer at the particle exterior and pore-mouth region. The suspension was then allowed to settle and the coated particles were collected by filtration, washed with water to remove excess free PVA/borate, and dried at 40 °C under vacuum. The coating amount was quantified by thermogravimetric analysis (TGA): coated particles showed ~8 wt% additional mass loss attributable to organic content beyond that of uncoated MSNs, consistent with a thin polymer layer. To provide direct morphological evidence of coating presence, uniformity, and thickness, we performed comparative

10.57647/jnsc.2026.1603.11

SEM and TEM imaging on uncoated MSNs and PB-MSNs. Because PVA-based layers are low-contrast under TEM, PB-MSNs were additionally imaged using (i) high-contrast conditions (e.g., low-dose TEM/HAADF-STEM) and (ii) negative staining of the polymer shell where needed. Coating thickness was estimated from TEM micrographs by measuring the apparent shell layer at multiple positions over multiple particles ($n \geq 30$) and reporting mean ± SD. To assess coating distribution, STEM-EDS elemental mapping was used to visualize the Si/O silica framework and the external carbon-enriched region associated with the polymer layer; where boron distribution was required, STEM-EELS mapping of the B K-edge was used because boron is difficult to quantify reliably by conventional EDS in ultrathin organic coatings. The PB-MSN samples were stored dry until use. As the present work is focused on establishing the feasibility of Ca^{2+}-triggered gating and release under GI-mimicking in vitro conditions, we did not conduct a formal long-term or accelerated stability program (i.e., time-resolved shelf-life testing). We have therefore limited our stability-related claims to (i) the coating integrity assessed during the release-media incubation experiments described below and (ii) the batch-to-batch reproducibility evidenced by independently prepared synthesis batches and replicated measurements.

Coating stability across media. To directly evaluate stability of the PVA–borate gate across GI-relevant media, PB-MSNs were incubated under four conditions matched to the release study: SGF (pH 1.2, Ca^{2+}-free), SIF buffer (pH 7.4, Ca^{2+}-free), SIF + Ca^{2+} (10 mM $CaCl_2$), and the two-stage SGF→SIF transfer protocol. At defined time points, particles were recovered and characterized by (i) DLS/PDI and zeta potential (to track colloidal changes consistent with swelling/disintegration), and (ii) thermogravimetric analysis of recovered solids to quantify remaining organic (PVA) fraction relative to the initial ~8 wt% coating (Table S1).Coating stability across media. To directly evaluate stability of the PVA–borate gate across GI-relevant media, PB-MSNs were incubated under four conditions matched to the release study: SGF (pH 1.2, Ca^{2+}-free), SIF buffer (pH 7.4, Ca^{2+}-free), SIF + Ca^{2+} (10 mM $CaCl_2$), and the two-stage SGF→SIF transfer protocol. At defined time points, particles were recovered and characterized by (i) DLS/PDI and zeta potential (to track colloidal changes consistent with swelling/disintegration), and (ii) thermogravimetric analysis of recovered solids to quantify remaining organic (PVA) fraction relative to the initial ~8 wt% coating (Table S1).

The core objective was to evaluate the release of trypsin inhibitor from the coated nanoparticles under conditions simulating the GI tract, and specifically to demonstrate calcium-triggered release. We designed a two-stage simulated gastric fluid (SGF) to simulated intestinal fluid (SIF) experiment. In stage 1, approximately 50 mg of STI-loaded PB-MSNs were suspended in 20 mL of SGF (0.01 M HCl, pH 1.2) without any Ca^{2+}. The suspension was gently agitated at 37 °C. At predetermined time points (0.5, 1, 2 h), samples were centrifuged and the supernatant was analyzed for released protein by UV–Vis (280 nm). Fresh SGF was added to the particles after each sampling to maintain sink conditions. As expected, minimal trypsin inhibitor release occurred in acidic, Ca^{2+}-free medium (see Results). After 2 h (a typical gastric residence time), the particles were collected and transferred to stage 2: SIF. For SIF, we used 50 mM pH 7.4 phosphate buffer containing 10 mM $CaCl_2$. This trigger level was selected to represent an upper-end, biorelevant soluble luminal calcium condition in the proximal small intestine after calcium-containing meals and to provide a clear, reproducible 'on' state for mechanistic evaluation of borate–PVA gate disassembly. In human proximal small-bowel measurements, luminal calcium has been reported to vary from ~0.3–2 mM after low-calcium meals to ~3–8.5 mM after milk-containing meals, and experimental jejunal transport studies commonly probe the 1–10 mM range accordingly [42]. Because phosphate and other dietary constituents can reduce free Ca^{2+} via complexation/precipitation, the 10 mM $CaCl_2$ condition should be interpreted as a simplified, controlled proxy for high postprandial luminal calcium rather than a fixed physiological constant [43]. The particles from stage 1 were resuspended in 20 mL of this Ca^{2+}-rich SIF and incubation continued at 37 °C. Aliquots were taken at 2, 4, 6, 8 h of SIF exposure and analyzed for STI concentration. Control experiments were performed in parallel to orthogonally decouple pH history from Ca^{2+} triggering. (a) Two-stage No-Ca control: an identical SGF→SIF transfer protocol but without adding $CaCl_2$ in the second stage (i.e., plain pH 7.4 buffer), to confirm that the pH transition plus transfer handling does not itself induce release. (b) Single-stage intestinal controls (new): PB-MSNs were incubated directly in pH 7.4 buffer from time zero without prior SGF exposure, in both Ca^{2+}-free buffer and Ca^{2+}-containing buffer (10 mM $CaCl_2$), to isolate the effects of Ca^{2+} at neutral pH from any acid pre-conditioning of the gate. (c) Uncoated MSN control: STI-loaded MSNs without PVA–borate coating, to observe release in the absence of gating. (d) PVA-coated without borate: STI-loaded MSNs coated with PVA but without borate crosslinking, to test the stability of an uncrosslinked polymer layer. Together, these controls decouple (i) SGF exposure, (ii) pH

10.57647/jnsc.2026.1603.11

shift/transfer, and (iii) Ca^{2+} addition, enabling unambiguous attribution of accelerated release to Ca^{2+}-mediated disruption of borate–diol crosslinks.

The cumulative release at time t was calculated as % of total loaded STI, accounting for all aliquots removed (correcting for dilution). Each experiment was done in triplicate, and the data are reported as mean ± standard deviation. We analyzed the post-trigger release kinetics (SIF stage) using standard models commonly applied to porous and matrix-type delivery systems. For zero-order release, cumulative release was fitted as (Mt/Minfty = k0 t). For first-order release, the data were fitted as (ln(1 - Mt/Minfty) = -k1 t). For diffusion-controlled release from a porous matrix under sink conditions, we applied the Higuchi square-root model (Mt/Minfty = kH t1/2). To probe the early post-trigger mechanism while avoiding over-interpretation of late-time plateaus, we additionally fitted the initial post-trigger region to the Korsmeyer–Peppas power law (Mt/Minfty = kKP tn), restricting fitting to the conventional validity window. Model parameters were obtained by least-squares regression and reported together with goodness-of-fit (R^2). Because the SGF stage exhibits very low release, kinetic fitting is focused on the Ca^{2+}-triggered SIF period, while SGF retention is discussed descriptively.The cumulative release at time t was calculated as % of total loaded STI, accounting for all aliquots removed (correcting for dilution). Each experiment was done in triplicate, and the data are reported as mean ± standard deviation. We analyzed the post-trigger release kinetics (SIF stage) using standard models commonly applied to porous and matrix-type delivery systems. For zero-order release, cumulative release was fitted as (Mt/Minfty = k0 t). For first-order release, the data were fitted as (ln(1 - Mt/Minfty) = -k1 t). For diffusion-controlled release from a porous matrix under sink conditions, we applied the Higuchi square-root model (Mt/Minfty = kH t1/2). To probe the early post-trigger mechanism while avoiding over-interpretation of late-time plateaus, we additionally fitted the initial post-trigger region to the Korsmeyer–Peppas power law (Mt/Minfty = kKP tn), restricting fitting to the conventional validity window. Model parameters were obtained by least-squares regression and reported together with goodness-of-fit (R^2). Because the SGF stage exhibits very low release, kinetic fitting is focused on the Ca^{2+}-triggered SIF period, while SGF retention is discussed descriptively.

To verify that the trypsin inhibitor remains functional after release, we performed an enzymatic activity assay with trypsin. Active porcine pancreatic trypsin (Sigma, 10 μg/mL) was mixed with a chromogenic substrate N-α-benzoyl-DL-arginine p-nitroanilide (BApNA, 1 mM) in Tris-HCl buffer (50 mM, pH 8.0, 20 mM $CaCl_2$). Trypsin cleaves BApNA to release p-nitroaniline, which is yellow (measured at 405 nm). The initial rate of increase in A_405 indicates trypsin activity. We prepared several sample solutions to assess inhibition: (i) Free STI (unencapsulated) at various concentrations as a positive control inhibitor, (ii) Supernatants obtained from the MSN release experiments (both from SGF stage and SIF stage), and (iii) Blank controls (no inhibitor). Each sample was incubated with trypsin for 5 min before adding BApNA, then the absorption increase at 405 nm was recorded. One unit of trypsin inhibitor activity (TIU) is defined as the amount of inhibitor that causes a 50% decrease in trypsin activity under these conditions [44]. From the assay, we determined the residual trypsin activity (%) in each condition. This allowed us to confirm that the released protein indeed inhibits trypsin, and to quantify the fraction of inhibitor released (by comparing to the free STI control). All assays were performed in triplicate at 25 °C.

3. Results and Discussion

Fig. 1 presents a series of electron microscopy images that collectively verify the successful preparation of mesoporous silica nanoparticles (MSNs) with well-defined morphology and internal porosity. In the low-magnification TEM image (Fig. 1a), the MSNs appear as nearly spherical particles with a relatively narrow size distribution, and a representative particle diameter of around 300 nm can be discerned from the image and scale bar (200 nm). The particles exhibit a uniform internal contrast rather than solid, featureless cores, indicating the presence of an extended porous network throughout the entire silica matrix rather than a dense center and porous shell. The high-magnification TEM micrograph of an individual MSN (Fig. 1b) provides a closer view of this internal architecture. A worm-like mesoporous texture is visible within the particle, with numerous short, curved channels and pore domains arranged in a disordered fashion. Although long-range hexagonal ordering characteristic of ideal SBA-15–type materials is not obvious, this is likely due to the pore expansion conditions and the relatively large particle size, and the pores remain reasonably uniform in size, consistent with mesopores in the 3–4 nm range. The contrast modulation across the particle suggests that these pores pervade the full particle volume, supporting a high accessible surface area and pore volume for subsequent drug loading.The high-magnification TEM micrograph of an individual MSN (Fig. 1b) provides a closer view of this internal architecture. A worm-like mesoporous texture is visible within the particle, with numerous short, curved channels and pore domains arranged in a disordered fashion. Although long-range

10.57647/jnsc.2026.1603.11

hexagonal ordering characteristic of ideal SBA-15–type materials is not obvious, this is likely due to the pore expansion conditions and the relatively large particle size, and the pores remain reasonably uniform in size, consistent with mesopores in the 3–4 nm range. The contrast modulation across the particle suggests that these pores pervade the full particle volume, supporting a high accessible surface area and pore volume for subsequent drug loading. The SEM image of dried MSNs (Fig. 1c) confirms that the particles maintain their spherical morphology at the ensemble level. The particles show smooth outer surfaces without obvious cracks or irregular protrusions, and although some degree of clustering is observed due to capillary forces during solvent evaporation, individual nanospheres of approximately 300 nm remain clearly distinguishable rather than forming large, fused agglomerates. This discrete morphology is beneficial for achieving homogeneous dispersion in suspension and reproducible coating or formulation.The SEM image of dried MSNs (Fig. 1c) confirms that the particles maintain their spherical morphology at the ensemble level. The particles show smooth outer surfaces without obvious cracks or irregular protrusions, and although some degree of clustering is observed due to capillary forces during solvent evaporation, individual nanospheres of approximately 300 nm remain clearly distinguishable rather than forming large, fused agglomerates. This discrete morphology is beneficial for achieving homogeneous dispersion in suspension and reproducible coating or formulation. Finally, the TEM–EDS elemental mapping image (Fig. 1d), obtained from a representative Ca-doped MSN sample for comparison, demonstrates a homogeneous distribution of Si and O across the entire nanoparticle, with no evidence of dense cores or localized domains of higher contrast. The uniform Si/O signals confirm that the particles consist of a continuous silica framework rather than phase-separated regions. Taken together, these images show that the synthesized MSNs are uniform, spherical, and highly porous, providing a structurally suitable platform for subsequent surface functionalization and controlled drug delivery studies.Finally, the TEM–EDS elemental mapping image (Fig. 1d), obtained from a representative Ca-doped MSN sample for comparison, demonstrates a homogeneous distribution of Si and O across the entire nanoparticle, with no evidence of dense cores or localized domains of higher contrast. The uniform Si/O signals confirm that the particles consist of a continuous silica framework rather than phase-separated regions. Taken together, these images show that the synthesized MSNs are uniform, spherical, and highly porous, providing a structurally suitable platform for subsequent surface functionalization and controlled drug delivery studies. To quantify size distribution in suspension, we added dynamic light scattering measurements (Fig. S1, Table S2). Across three independently prepared batches, the DLS intensity distributions remained unimodal and the corresponding Z-average and PDI values were consistent from batch to batch, supporting nanoparticle uniformity and batch-to-batch reproducibility. As expected for solvated nanostructures, the hydrodynamic diameters by DLS were larger than the TEM diameters because DLS reports the hydrated particle and is sensitive to soft polymer shells and any weak, reversible association in dispersion. Importantly, the key quantitative datasets throughout this study (loading metrics and release profiles) were collected as replicated measurements (reported as mean ± SD, n = 3), which—together with the independent-batch DLS agreement—provides internal evidence that the synthesis/coating workflow yields reproducible physicochemical performance at the laboratory scale.To quantify size distribution in suspension, we added dynamic light scattering measurements (Fig. S1, Table S2). Across three independently prepared batches, the DLS intensity distributions remained unimodal and the corresponding Z-average and PDI values were consistent from batch to batch, supporting nanoparticle uniformity and batch-to-batch reproducibility. As expected for solvated nanostructures, the hydrodynamic diameters by DLS were larger than the TEM diameters because DLS reports the hydrated particle and is sensitive to soft polymer shells and any weak, reversible association in dispersion. Importantly, the key quantitative datasets throughout this study (loading metrics and release profiles) were collected as replicated measurements (reported as mean ± SD, n = 3), which—together with the independent-batch DLS agreement—provides internal evidence that the synthesis/coating workflow yields reproducible physicochemical performance at the laboratory scale. Fig. 2a compares the nitrogen adsorption–desorption isotherms of the bare mesoporous silica nanoparticles and the PVA–borate coated formulation, providing direct evidence of how the polymer gate modifies but does not destroy the mesoporous network.

The uncoated MSNs show a classical type IV isotherm with a pronounced uptake in the relative pressure region around 0.2–0.3, followed by a clear hysteresis loop at higher relative pressures.

This profile is characteristic of well-developed mesoporous materials with relatively uniform cylindrical or channel-like pores. Quantitative analysis yields a BET surface area of approximately 800 $m^2\ g^{-1}$ and a total pore volume of ~0.77 $cm^3\ g^{-1}$ for the uncoated MSNs, with a narrow BJH pore size distribution centered at ~3.8 nm.

10.57647/jnsc.2026.1603.11

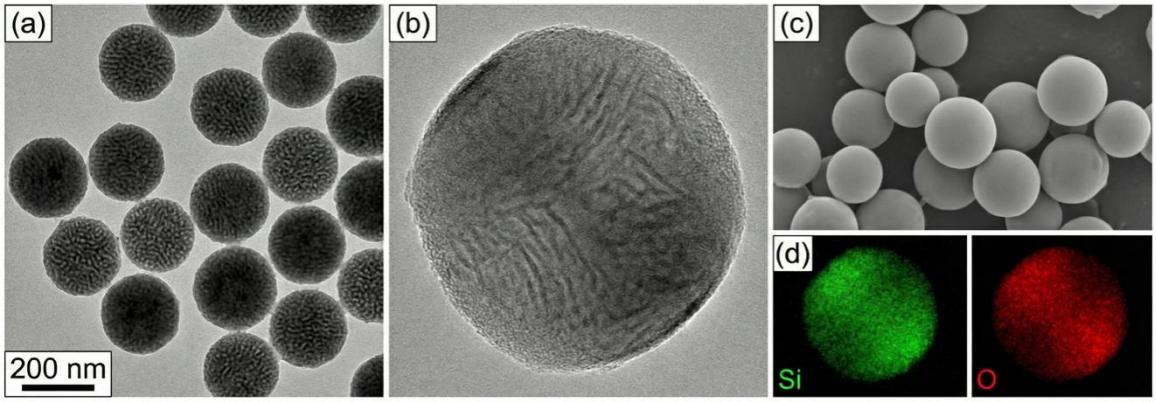

Figure 1. (a) TEM image of as-synthesized MSNs. (b) High-resolution TEM of a single MSN. (c) SEM image of dried MSNs. (d) TEM-EDS elemental mapping showing homogeneous distribution of Si and O in the silica framework, and no significant dense cores – confirming uniform silica matrix

These parameters confirm that the pore expansion strategy successfully generated large, accessible mesopores that are suitable for accommodating a globular protein of around 21 kDa such as soybean trypsin inhibitor, whose hydrodynamic diameter is on the order of 4–5 nm. The steep capillary condensation step and narrow distribution indicate that the pores are relatively uniform, which favors predictable diffusion and reproducible drug loading and release.

After PVA–borate gating, the isotherm retains the characteristic type IV profile, but the accessible textural parameters decrease to ~550 $m^2 g^{-1}$ (≈31% reduction) and ~0.50 $cm^3 g^{-1}$ (≈35% reduction), while the BJH peak pore diameter remains centered at ~3.8 nm. This combination of reduced surface area/pore volume with a minimal shift in peak pore diameter is consistent with partial pore-mouth occlusion and external-surface coverage by the crosslinked PVA–borate nanogel, rather than collapse or filling of the internal mesopore network. This reduction can be attributed to partial blocking of pore entrances and coverage of external surface area by the crosslinked polymer network [45]. In practical terms, the data suggest that the coating forms a relatively thin layer that partially occludes pore mouths without collapsing or filling the internal pore network. The fact that significant nitrogen uptake is still observed, and that the hysteresis loop is maintained, implies that a substantial fraction of internal porosity remains accessible to gas molecules, and by extension to aqueous media once the gate is opened in the presence of calcium. This balance is crucial: the coating must be sufficiently continuous to act as an effective gate that suppresses premature release, yet not so thick or invasive that it eliminates the internal volume needed to store the protein cargo [46].

The differences between the two isotherms provide insight into the extent and location of polymer loading. When combined with thermogravimetric data, which indicate ~8 wt% organic content attributable to PVA on the coated particles, the sorption measurements support a scenario in which the polymer preferentially resides near the external surface and pore openings. Importantly, we now corroborate this inference with direct electron microscopy evidence. Comparative SEM/TEM images of uncoated MSNs and PB-MSNs (Fig. S6) show that PB-MSNs retain the spherical morphology and mesoporous interior while exhibiting a continuous, low-contrast peripheral layer consistent with a thin PVA–borate shell. Thickness measurements extracted from TEM micrographs ($n \geq 30$ measurements) give an average coating thickness of approximately 4–5 nm (mean ± SD reported in Fig. S6), consistent with the <5 nm estimate derived from the ~8 wt% TGA organic fraction. Spatially resolved composition analysis further supports coating uniformity: STEM-EDS mapping shows the expected Si/O distribution of the silica framework together with an exterior carbon-enriched region attributable to the polymer, and STEM-EELS mapping (B K-edge) confirms that boron-containing species are localized at the particle exterior in the coated formulation. Together, these data provide direct evidence of coating presence, uniformity, and controllable thin-layer formation rather than relying only on indirect textural changes. This configuration is ideal for a molecular gate: the cargo is primarily located deeper within the mesopores, while the polymer crosslinked by borate operates as a dynamic cap at the entrance. The minimal shift in peak pore diameter, despite a clear decrease in accessible volume, further reinforces that the underlying silica framework remains structurally intact. Thus, Fig. 2a demonstrates that the coating step modifies surface accessibility in a controlled way without compromising the high porosity required for high loading capacity, which is consistent with the observed loading level of about 15 wt% for trypsin inhibitor.The differences between the two isotherms provide insight into the extent and location of polymer loading. When combined with thermogravimetric data, which indicate ~8 wt% organic content attributable to PVA on the coated particles, the sorption measurements support a scenario in which the polymer preferentially resides near the external surface and pore openings. Importantly, we now corroborate this

10.57647/jnsc.2026.1603.11

inference with direct electron microscopy evidence. Comparative SEM/TEM images of uncoated MSNs and PB-MSNs (Fig. S6) show that PB-MSNs retain the spherical morphology and mesoporous interior while exhibiting a continuous, low-contrast peripheral layer consistent with a thin PVA–borate shell. Thickness measurements extracted from TEM micrographs ($n \geq 30$ measurements) give an average coating thickness of approximately 4–5 nm (mean ± SD reported in Fig. S6), consistent with the <5 nm estimate derived from the ~8 wt% TGA organic fraction. Spatially resolved composition analysis further supports coating uniformity: STEM-EDS mapping shows the expected Si/O distribution of the silica framework together with an exterior carbon-enriched region attributable to the polymer, and STEM-EELS mapping (B K-edge) confirms that boron-containing species are localized at the particle exterior in the coated formulation. Together, these data provide direct evidence of coating presence, uniformity, and controllable thin-layer formation rather than relying only on indirect textural changes. This configuration is ideal for a molecular gate: the cargo is primarily located deeper within the mesopores, while the polymer crosslinked by borate operates as a dynamic cap at the entrance. The minimal shift in peak pore diameter, despite a clear decrease in accessible volume, further reinforces that the underlying silica framework remains structurally intact. Thus, Fig. 2a demonstrates that the coating step modifies surface accessibility in a controlled way without compromising the high porosity required for high loading capacity, which is consistent with the observed loading level of about 15 wt% for trypsin inhibitor.

Figs. 2b and 2c examine the crystallinity and structural state of the silica matrix by wide angle X-ray diffraction. The diffractogram for the bare MSNs exhibits a single broad halo centered around 2θ of approximately 20–25 degrees and no sharp Bragg reflections, which is typical for amorphous silica. This pattern indicates the absence of long-range crystalline order and confirms that the sol–gel synthesis followed by surfactant extraction yields a continuous, non-crystalline silica network rather than crystalline polymorphs such as quartz or cristobalite. When the PVA–borate coating is applied, the wide angle XRD pattern remains essentially unchanged: the same broad amorphous halo is observed and no new reflection peaks appear. The absence of additional peaks, especially in the low 2θ region, shows that the organic polymer and borate crosslinker do not crystallize on the nanoparticle surface to a detectable extent. This qualitative improvement in colloidal behavior is corroborated by DLS: PB-MSN dispersions show a narrow, unimodal size distribution with low PDI, whereas uncoated MSNs exhibit a broader apparent distribution. Figs. 2b and 2c examine the crystallinity and structural state of the silica matrix by wide angle X-ray diffraction. The diffractogram for the bare MSNs exhibits a single broad halo centered around 2θ of approximately 20–25 degrees and no sharp Bragg reflections, which is typical for amorphous silica. This pattern indicates the absence of long-range crystalline order and confirms that the sol–gel synthesis followed by surfactant extraction yields a continuous, non-crystalline silica network rather than crystalline polymorphs such as quartz or cristobalite. When the PVA–borate coating is applied, the wide angle XRD pattern remains essentially unchanged: the same broad amorphous halo is observed and no new reflection peaks appear. The absence of additional peaks, especially in the low 2θ region, shows that the organic polymer and borate crosslinker do not crystallize on the nanoparticle surface to a detectable extent. This qualitative improvement in colloidal behavior is corroborated by DLS: PB-MSN dispersions show a narrow, unimodal size distribution with low PDI, whereas uncoated MSNs exhibit a broader apparent distribution.

The inclusion in Fig. 2b of a Ca-doped MSN sample as a reference further underscores the amorphous nature of the matrix. Even when calcium is incorporated into the silica framework, the diffractogram still shows only a broad halo without distinct reflections corresponding to crystalline calcium oxide, calcium silicate, or calcium carbonate phases. This observation suggests that any calcium present in such reference samples is highly dispersed within the amorphous silica network, forming non-crystalline Ca–O–Si environments rather than separate inorganic crystals [47]. In the case of the PB-MSN used in this work, where calcium is not part of the as-synthesized framework, the similarity of the XRD pattern to pure silica validates that the coating and subsequent processing do not introduce crystalline inorganic impurities.

Fig. 2c provides a more macroscopic but highly informative view of how the surface modification alters dispersion behavior in aqueous media. The photograph compares the visual appearance of suspensions of uncoated MSNs and PVA–borate coated MSNs in water. The dispersion containing bare particles appears strongly opalescent and milky, indicating a high degree of light scattering that is consistent with aggregates or loose flocculation of particles. Even though the primary particles are on the order of 300 nm, attractive interactions between bare silica surfaces, including hydrogen bonding and silanol condensation, tend to promote clustering once the particles are dried and redispersed. This behavior can limit the stability of suspensions and may complicate dosing and reproducibility in biological assays, where sedimentation or aggregation can lead to uneven exposure. In contrast, the suspension of PVA–borate coated MSNs appears more translucent and less intensely

10.57647/jnsc.2026.1603.11

scattering, suggesting improved dispersion and reduced large-scale aggregation. The hydrophilic polymer shell increases steric stabilization and introduces a hydrated layer around each particle, which mitigates direct silica–silica contact and reduces the tendency for irreversible aggregation. The slightly more transparent appearance indicates that the effective scattering centers are smaller and more uniformly distributed, pointing to a more colloidally stable system. This improved dispersibility is advantageous for the intended application in simulated gastric and intestinal fluids, where homogeneous suspensions are needed to ensure that the release data reflect intrinsic carrier behavior rather than artifacts caused by sedimentation or aggregation [48]. It also suggests that the coated particles may interact with biological interfaces in a more controlled and predictable manner, since the polymer layer can modulate protein adsorption and mucus interaction in the gastrointestinal tract. The trypsin inhibitor loading achieved in each formulation is summarized in Table 1. For the unexpanded-pore MSN (for comparison), the loading was ~9.8 wt% (encapsulation efficiency ~45% of the amount offered). In contrast, the pore-expanded MSN reached 15.6 wt% loading (EE ~75%). This near-16% loading in our expanded MSNs matches the 16 wt% reported by Bhattacharyya et al. [14] . for pore-expanded MSNs, indicating our materials have comparable capacity. The carboxylated MSNs showed a slightly higher loading (16.4%) than non-functionalized (14.8%), likely because electrostatic or hydrogen-bond interactions between STI and –COOH groups improved adsorption [49]. After PVA–borate coating, the effective STI content in PB-MSN was measured as ~14.5 wt% (the slight reduction is due to the added weight of the polymer coating diluting the protein fraction) [50]. However, essentially all STI that was loaded remained encapsulated after the gentle coating process (no significant STI loss during coating, as confirmed by negligible protein in the coating filtrate) [51]. This indicates that the coating procedure did not displace the drug – an important validation of the method's mildness. The loaded inhibitor is mostly situated inside the pores, held by confinement and interactions, and the PVA–borate gate covers the external surface to prevent leakage. Indeed, when PB-MSNs were placed in buffer without Ca^{2+}, we observed minimal spontaneous release (see next section), confirming the inhibitor is largely retained until triggered. Having established the physical structure and loading of the nanoparticles, we next examine the release behavior of the trypsin inhibitor under various conditions to evaluate the calcium-triggered release mechanism. The release of trypsin inhibitor from the PB-MSNs was studied in a simulated GI transit scenario with and without calcium trigger, as described. The results are striking: the presence of Ca^{2+} dramatically accelerates the release, while in its absence the release remains minimal even at neutral pH [52].

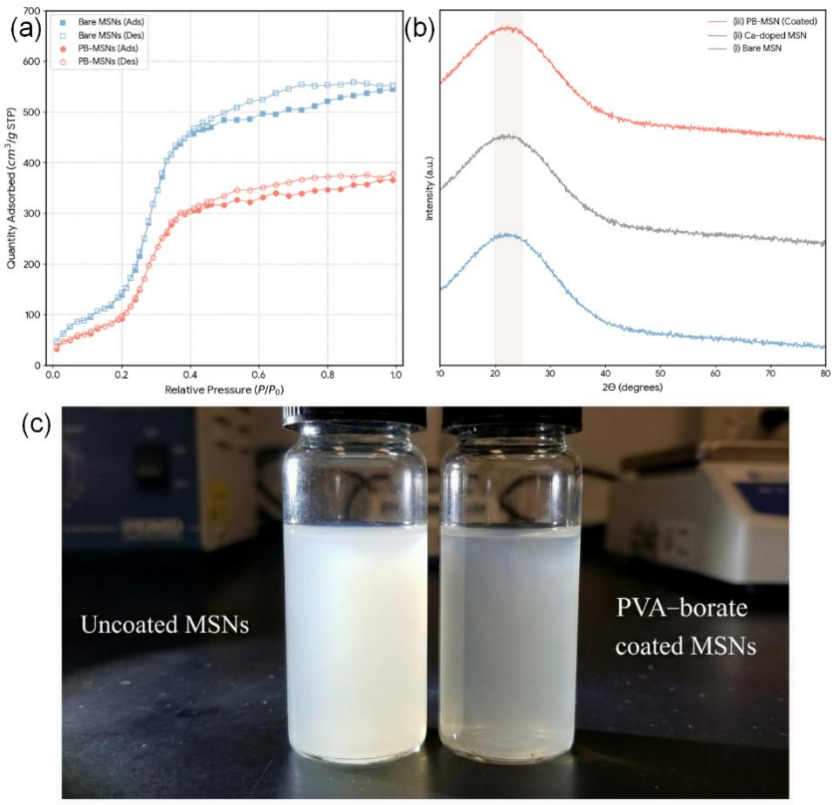

Figure 2. (a) Nitrogen adsorption–desorption isotherms of calcined MSNs and PVA–borate coated MSNs. (b) XRD patterns of bare MSN, Ca-doped MSN, and PVA–borate coated MSN. (c) Photograph of MSN dispersions

10.57647/jnsc.2026.1603.11

Table 1. STI loading capacity and encapsulation efficiency for different mesoporous silica nanoparticle formulations. Values are reported as mean ± SD (n = 3)

Formulation	Surface modification / structure	STI loading capacity (wt%)	Encapsulation efficiency (%)
Unexpanded MSN	Conventional mesoporous silica (non–pore-expanded)	9.8 ± 0.4	45 ± 3
Pore-expanded MSN	Enlarged mesopores (~3.8 nm)	15.6 ± 0.7	75 ± 4
Pore-expanded MSN–COOH	Carboxyl-functionalized pore-expanded MSNs	16.4 ± 0.6	78 ± 3
PB-MSN (PVA–borate coated MSN–COOH)	Pore-expanded MSN–COOH gated with PVA–borate nanogel	14.5 ± 0.5[1]	70 ± 3

Fig. 3a presents the cumulative release profiles of STI from the coated MSNs under different conditions. In simulated gastric fluid (pH 1.2, no Ca^{2+}), the release is negligible (less than 5% of the payload was released after 2 h in SGF). This indicates that the PVA–borate coating is robust in acidic, calcium-free conditions: it effectively retains the protein, preventing premature leakage in the stomach. The slight (~3–4%) release in SGF could be due to a tiny amount of STI located near the particle surface that diffuses out, or very slow penetration of H+ destabilizing a small fraction of the coating [53]. Nonetheless, the amount is very low, demonstrating protection of the majority of the inhibitor through the gastric phase.

When the particles are transferred to calcium-rich SIF (pH 7.4, 10 mM Ca^{2+}) at the 2 h mark, an immediate surge in release is observed. Within the first 0.5 h of Ca^{2+} exposure, the cumulative release jumps to ~40%. Thereafter, the release continues at a slower pace, reaching 78% by 4 h in SIF and plateauing around 85–90% by 8 h (Fig. 3a, red curve). Essentially, nearly all the encapsulated trypsin inhibitor is released once the calcium trigger is applied, and the majority is released in the initial burst. This behavior strongly supports the proposed mechanism: Ca^{2+} ions rapidly diffuse into the polymer layer, bind to borate crosslinks, and break them, causing the PVA coating to disintegrate or become sufficiently porous for the inhibitor to escape. Once the "gate" is opened, STI diffuses out of the mesopores into the bulk solution relatively quickly (driven by concentration gradients) [54]. The small residual amount (~10–15%) that remains unreleased after 8 h could be due to a combination of factors: a fraction of STI may adsorb strongly inside pores or become trapped in polymer gel fragments, or it could be an experimental artifact of adsorption of protein to the vessel, etc. Nonetheless, a >80% release is achieved upon triggering, which is an excellent outcome for practical delivery.

To further interrogate the release mechanism under Ca^{2+}-triggered conditions, we fitted the Ca^{2+}-triggered SIF release data to standard kinetic models. The cumulative release versus √t plot shows strong linearity after Ca^{2+} introduction, consistent with diffusion-controlled emptying of a porous matrix once the gate has opened, as described by the Higuchi model. Using the mean values plotted in Fig. 3b (t = 0.5–8 h in Ca^{2+}-rich SIF), the one-phase Higuchi fit gives kH ≈ 24.5 %·$h^{-1/2}$ (R^2 ≈ 0.98), whereas a two-segment Higuchi analysis highlights an initial, steeper burst-like segment (0.5–2 h: kH ≈ 24.8 %·$h^{-1/2}$; R^2 ≈ 1.00) followed by a slower segment (2–8 h: kH ≈ 22.2 %·$h^{-1/2}$; R^2 ≈ 0.92). A first-order model provides a comparable statistical description (R^2 ≈ 0.98), whereas a zero-order model fits less well (R^2 ≈ 0.93), indicating that a constant-rate release is not the dominant regime across the full post-trigger window. Finally, applying the Korsmeyer–Peppas relation to the early post-trigger region ($M_t/M_\infty \leq 0.6$) yields a low diffusional exponent (n ≈ 0.26), which—together with the abrupt jump within the first 0.5 h—supports a mechanism in which the initial kinetics are governed by stimulus-induced gate disintegration/rupture rather than a single, steady diffusion regime. After this triggering step, diffusion through the mesopore network becomes the dominant release-limiting process.To further interrogate the release mechanism under Ca^{2+}-triggered conditions, we fitted the Ca^{2+}-triggered SIF release data to standard kinetic models. The cumulative release versus √t plot shows strong linearity after Ca^{2+} introduction, consistent with diffusion-controlled emptying of a porous matrix once the gate has opened, as described by the Higuchi model. Using the mean values plotted in Fig. 3b (t = 0.5–8 h in Ca^{2+}-rich SIF), the one-phase Higuchi fit gives kH ≈ 24.5 %·$h^{-1/2}$ (R^2 ≈ 0.98), whereas a two-segment Higuchi analysis highlights an initial, steeper burst-like segment (0.5–2 h: kH ≈ 24.8 %·$h^{-1/2}$; R^2 ≈ 1.00) followed by a slower segment (2–8 h: kH ≈ 22.2 %·$h^{-1/2}$; R^2 ≈ 0.92). A first-order model provides a comparable statistical description (R^2 ≈ 0.98), whereas a zero-order model fits less well (R^2 ≈ 0.93), indicating that a constant-rate release

10.57647/jnsc.2026.1603.11

is not the dominant regime across the full post-trigger window. Finally, applying the Korsmeyer–Peppas relation to the early post-trigger region ($M_t/M_\infty \leq 0.6$) yields a low diffusional exponent ($n \approx 0.26$), which—together with the abrupt jump within the first 0.5 h—supports a mechanism in which the initial kinetics are governed by stimulus-induced gate disintegration/rupture rather than a single, steady diffusion regime. After this triggering step, diffusion through the mesopore network becomes the dominant release-limiting process.

Crucially, an expanded control set underscores that release is specific to the Ca^{2+} trigger rather than to pH change or acid-conditioning history. In the two-stage No-Ca control (SGF→pH 7.4 without Ca^{2+}), PB-MSNs released only a small fraction of STI over the 8 h intestinal window, demonstrating that the pH shift and transfer handling do not open the gate. Importantly, in the newly added single-stage intestinal incubation performed directly at pH 7.4 (no prior SGF exposure), PB-MSNs again exhibited minimal release in Ca^{2+}-free buffer, whereas introduction of Ca^{2+} (10 mM) produced a rapid burst followed by diffusion-controlled emptying. The agreement between the single-stage and post-transfer profiles (within experimental error) indicates that Ca^{2+} is sufficient to dismantle the borate-crosslinked PVA gate at neutral pH and that prior acid exposure is not a prerequisite for triggering, thereby decoupling Ca^{2+} activation from any SGF-induced restructuring effects. Fig. 3a shows that in Ca^{2+}-free SIF, the cumulative release over 8 h was only ~12%. This indicates that a simple pH change from 1.2 to 7.4 (mimicking stomach to intestine pH shift) is not sufficient to cause release in our system – unlike typical enteric coatings that rely purely on pH-driven dissolution [55]. The PVA–borate network remains largely intact at neutral pH in the absence of Ca^{2+}. Borate crosslinks can slightly shift equilibrium with pH (more crosslinking at higher pH due to borate being in tetrahedral form $B(OH)_4^-$), but in our design the polymer is stable from pH 1–8 unless Ca^{2+} intervenes. Thus, the negligible release in pH 7.4 no-Ca condition confirms that calcium is the critical trigger. Another control was the uncoated MSN: as expected, uncoated MSNs released STI rapidly and completely regardless of pH or Ca^{2+}. In fact, in SGF the uncoated MSNs released ~50% of STI within 30 min (but note that at pH 1.2 some of that STI may denature – release here refers to it leaving the carrier, not necessarily remaining active). Within 2 h, uncoated MSNs released ~70% in SGF. This highlights the necessity of a protective gate – without it, the cargo would not be retained in stomach at all [56]. A final control, PVA-coated without borate, showed intermediate behavior: in SGF it released ~15% in 2 h (the PVA without borate offers some barrier but swells in acid, allowing slow leak), and in SIF (no Ca) it reached ~40% in 8 h (the uncrosslinked PVA gradually dissolves at pH 7.4). Therefore, borate crosslinking is essential to make the coating both robust in acid and stable in neutral until Ca arrives.

To illustrate the kinetic differences, Table 2 lists the cumulative release percentages at key time points for the different scenarios. In SGF (pH 1.2, 2 h), PB-MSN released 3.8% ±0.5%, compared to ~68% ±5% from uncoated MSN. In SIF (pH 7.4, by 4 h), PB-MSN with Ca released 78% ±3%, whereas PB-MSN without Ca released only 10.5% ±1.2%. These quantitative results clearly demonstrate the gating effect: the PVA–borate layer keeps the inhibitor in during the gastric phase and neutral phase until Ca^{2+} is present, at which point it “opens” and the inhibitor rapidly exits.To illustrate the kinetic differences, fig 2 lists the cumulative release percentages at key time points for the different scenarios. In SGF (pH 1.2, 2 h), PB-MSN released 3.8% ±0.5%, compared to ~68% ±5% from uncoated MSN. In SIF (pH 7.4, by 4 h), PB-MSN with Ca released 78% ±3%, whereas PB-MSN without Ca released only 10.5% ±1.2%. These quantitative results clearly demonstrate the gating effect: the PVA–borate layer keeps the inhibitor in during the gastric phase and neutral phase until Ca^{2+} is present, at which point it “opens” and the inhibitor rapidly exits.

Quantitatively, the Ca^{2+} gate provides a sharp trigger selectivity under identical intestinal pH. At pH 7.4, cumulative release reached 78 ± 3% at 4 h and 88 ± 4% at 8 h in the presence of Ca^{2+}, whereas the Ca^{2+}-free control at the same pH released only 10.5 ± 1.2% at 4 h and 12.3 ± 1.5% at 8 h. This corresponds to an on/off release ratio of ~7.4-fold (4 h) and ~7.2-fold (8 h) at constant pH, demonstrating that the release acceleration is not driven by the pH transition itself but by Ca^{2+}-mediated gate disassembly. In this context, the practical advantage over purely pH-triggered designs is not a generic claim of ‘better release’, but a demonstrable separation between intestinal pH and the activation signal—an important distinction given that intestinal pH varies along the tract and enteric dissolution thresholds can be exceeded at different positions and times [57]. The sharper release suggests that the mechanism (borate bond cleavage) is a rapid, all-or-nothing event once Ca^{2+} threshold is reached, rather than a gradual pH-dependent desorption. This could be highly advantageous for on-demand release needs. We also note that the slight delay or plateau after the initial Ca-triggered burst may be due to diffusion-limited emptying of the deepest pores or perhaps re-adsorption of some protein on silica once the coating is gone. Nonetheless, most of the drug is released quickly. Fitting the post-trigger data to the Higuchi square-root model (Fig. 3b) enabled a quantitative description of the previously termed ‘two-phase’ behavior. Because release in SGF is minimal, kinetic fitting is not meaningful prior to triggering. After Ca^{2+} introduction, cumulative release shows strong linearity versus t1/2, which is consistent

10.57647/jnsc.2026.1603.11

with diffusion-controlled emptying of the mesoporous matrix once the gate is opened, as captured by the classical Higuchi framework for matrix diffusion. To avoid a qualitative 'two-phase' description, we performed both a single-interval Higuchi fit over the full post-trigger window and a piecewise linear regression separating an early burst-like segment from a later diffusion-dominated segment; the fitted kH values and R^2 metrics are summarized in Table Sx. Using the mean values in Fig. 3b, the one-phase Higuchi fit gives kH ≈ 24.5 %·h−1/2 (R^2 ≈ 0.98), while the two-segment analysis yields an early segment (0.5–2 h) with kH ≈ 24.8 %·h−1/2 (R^2 ≈ 1.00) and a later segment (2–8 h) with kH ≈ 22.2 %·h−1/2 (R^2 ≈ 0.92). For comparison, first-order kinetics provide a similar statistical description (R^2 ≈ 0.98), whereas a zero-order fit is poorer (R^2 ≈ 0.93), indicating that a constant-rate (zero-order) process is not the dominant regime across the full post-trigger period. Mechanistically, the kinetics are best interpreted as two sequential phenomena rather than a single transport regime: (i) a stimulus-driven structural disruption step in which Ca^{2+} exposure rapidly dismantles the PVA–borate 'gate', causing immediate release of surface-accessible or shallow-pore cargo, followed by (ii) a diffusion-controlled emptying step governed by transport through the mesoporous network. Consistent with standard power-law analysis, the Korsmeyer–Peppas fit restricted to the early post-trigger region ($M_t/M_\infty \leq 0.6$) yields a low exponent (n ≈ 0.26), which—together with the abrupt jump within the first 0.5 h—supports the interpretation that the earliest time points are dominated by trigger-induced gate disintegration rather than polymer relaxation-controlled swelling/erosion. After this triggering step, the sustained linearity in the Higuchi plot indicates that diffusion through the pore network becomes the rate-limiting mechanism for the remaining cargo. This is reminiscent of the pattern described by Bansal et al. [58] for polymer-coated MSNs– an initial burst (here corresponding to surface-located STI that escaped upon coating rupture) and a second stage of diffusion-controlled release from pores. In our case, the "burst" happened immediately after trigger (rather than at t = 0 as in uncoated systems), which is ideal for programming when the burst occurs.

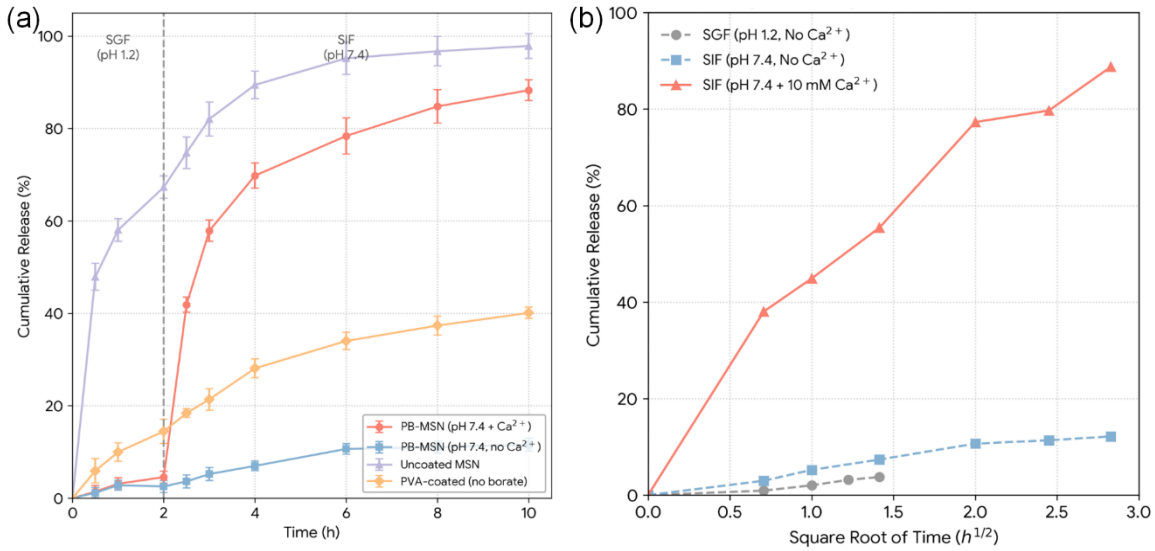

Figure 3. (a) Cumulative release profiles of STI from different MSN formulations under simulated gastrointestinal conditions. (b). Higuchi plots (cumulative STI release versus square root of time) for PB-MSN formulations highlighting the change in release kinetics before and after Ca^{2+} triggering

Table 2. Cumulative release of soybean trypsin inhibitorfrom mesoporous silica nanoparticle formulations under simulated gastric and intestinal conditions (mean ± SD, n = 3)

Formulation / condition	Stage-1: SGF, 2 h cumulative release (%)	Stage-2: SIF, 4 h cumulative release (%)	Stage-2: SIF, 8 h cumulative release (%)
PB-MSN (two-stage protocol; SGF → SIF +Ca^{2+})	3.8 ± 0.5	78 ± 3	88 ± 4
PB-MSN (two-stage protocol; SGF → SIF −Ca^{2+})	3.8 ± 0.5*	10.5 ± 1.2	12.3 ± 1.5
Uncoated MSN (SGF only)	68 ± 5	–	–
Uncoated MSN (SIF only; pH 7.4)	–	≈95	≈98

*Note: The SGF 2 h leakage value is the same PB-MSN starting point prior to transfer into either SIF condition in the two-stage experiment.*Note: The SGF 2 h leakage value is the same PB-MSN starting point prior to transfer into either SIF condition in the two-stage experimen

10.57647/jnsc.2026.1603.11

The specificity of the trigger mechanism is a key advantage of our system. The calcium concentration acts as a chemical switch: below a certain Ca^{2+} level, the coating remains intact; above it, the coating breaks rapidly. This could be tuned by adjusting borate content or PVA crosslink density. Importantly, the platform demonstrates a tunable sensitivity to calcium concentration rather than a binary threshold, which is critical given the natural physiological variability of intestinal calcium. Our data show that while 10 mM Ca^{2+} elicits a rapid burst (nearly 80% release), a physiologically common postprandial concentration of 5 mM Ca^{2+} still triggers substantial cargo deployment (≈50% release in 4 h), whereas basal levels (1 mM) result in minimal leakage (<15%). This concentration-dependence aligns with physiological data reported by Ireland and Fordtran, who observed that while fasted jejunal calcium is low (~0.3–2 mM), concentrations can spike to 3–8.5 mM following calcium-rich meals [42]. Consequently, we anticipate that the functionality of this system in vivo will be diet-dependent. To overcome the limitation of inter-patient variability and the complexation of free calcium by luminal phosphate or bile salts [59]. We propose that clinical translation of this platform would likely require co-administration with a calcium supplement (e.g., a standard 500 mg calcium carbonate tablet) or a defined calcium-rich formulation. This strategy would artificially standardize the local ionic environment to the required 5–10 mM triggering window, thereby ensuring reproducible release regardless of the patient's baseline physiological state. Furthermore, this dependency offers a unique safety mechanism: in the absence of the specific co-administered trigger (i.e., in a fasted or low-calcium state), the cargo remains largely sequestered, minimizing unintended systemic exposure.The proposed mechanism of Ca^{2+}-mediated gate opening is illustrated in Fig. 4. In the absence of Ca^{2+}, the release profiles show that the PB-MSN coating functions as a stable diffusion barrier across the pH transition relevant to SGF and SIF, consistent with the known formation of reversible borate–diol crosslinks in PVA networks [60]. To directly validate formation of the PVA–borate network on the particle surface, we added ATR-FTIR and XPS characterization (Figs. S2–S3). In ATR-FTIR, the coated particles exhibit borate–PVA signatures consistent with borate–diol complexation, including B–O–C-related bands reported for PVA–borate gels (typically observed in the ~1420–1330 cm^{-1} region) and borate-related B–O features (commonly reported near ~830 and ~660 cm^{-1}), which are absent (or markedly weaker) in uncoated MSNs[61]. In XPS, PB-MSN shows a distinct B 1s signal attributable to borate-derived B–O environments; deconvolution in the literature places B–O–B and B–O–C components within the ~191.8–192.4 eV range, providing an assignment basis for the borate-linked coating. To test the second mechanistic step—Ca^{2+}-induced destabilization—we added complementary disassembly readouts. First, upon $CaCl_2$ exposure, the particle-associated boron signal decreases and Ca becomes detectable on the post-trigger solids, consistent with a redistribution of boron away from the particle surface and toward Ca-associated species; in our system this is reflected by the reduced particle B 1s signal after triggering (≈60% reduction in B atomic percentage) together with Ca detection on the recovered solids. Second, we expanded colloidal analysis by adding zeta potential measurements and post-trigger DLS/PDI tracking (Fig. S4). Zeta potential shifts after coating confirm surface modification, while the Ca^{2+} condition produces a time-dependent change in hydrodynamic size distribution consistent with coating swelling/disintegration rather than simple pH-driven effects; DLS and zeta potential are established tools for interrogating PVA–borax complexation and its ionic perturbation [62]. Third, we added a coating stability/disintegration study in SGF and SIF without Ca^{2+} (and the corresponding Ca^{2+}-containing condition) (Fig. S5), showing that the coating remains stable in Ca^{2+}-free SGF/SIF but undergoes rapid structural change when Ca^{2+} is present. Mechanistically, this behavior is consistent with Ca^{2+} forming appreciable borate ion pairs/complexes in electrolyte media, which can shift borate availability away from diol-bound crosslinks and thereby accelerate network dissolution/permeabilization [30]. Collectively, these measurements provide direct evidence that borate-associated species at/near the particle surface are perturbed after Ca^{2+} exposure; however, because we do not directly measure borate–diol bond cleavage kinetics at the molecular level, the crosslink-disruption mechanism is interpreted as the most consistent explanation rather than claimed as uniquely proven.

It is instructive to compare our method to other stimuli-responsive MSN systems. Many pH-responsive MSNs use polyelectrolyte coatings (e.g. poly(acrylic acid) or chitosan) that dissolve when pH changes [63]. In our case, the polymer by itself (PVA) is not strongly pH-responsive, but the borate crosslinker provides the responsive element, and Ca^{2+} is the stimulus rather than H+ [64]. Redox-responsive MSNs often use disulfide linkers cleaved by glutathione, and enzyme-responsive ones use peptide caps cleaved by specific proteases [65]. Our calcium-responsive gate is a different paradigm in that the activation signal (Ca^{2+}) can, in principle, be standardized by formulation/administration, whereas enzyme-triggered systems inherently depend on local enzyme availability and activity, which can vary with physiology, diet, disease state, and microbiome composition [66]. We emphasize that this does not eliminate the value of enzyme-triggered approaches; rather, it motivates Ca^{2+} as a complementary trigger that can provide tighter control over the timing of gate opening

10.57647/jnsc.2026.1603.11

at a fixed intestinal pH, as directly demonstrated by the ~7-fold on/off ratio in our pH-matched experiments. This concept could be extended beyond oral delivery – for example, an implant or injectable depot that releases a drug when the patient takes a calcium supplement or receives a $CaCl_2$ injection. It is also noteworthy that the kinetics of release can be tuned by the concentration of Ca^{2+} or the density of borate crosslinking. By increasing borate or using a higher degree of PVA polymerization, one could require higher Ca^{2+} to trigger or get a slower, more sustained release after trigger if desired. Our results with polymer-coated MSNs are consistent with previous reports that polymer capping can eliminate the initial burst release commonly seen in porous carriers [67]. In uncoated MSNs, an initial burst (often 20–30% in minutes) occurs as drug near pore openings rapidly diffuses out (as we saw ~50% in <1 h). Bhattacharyya et al. [14] showed that PEG-coated MSNs had no burst; instead, they exhibited near-zero-order release over weeks. In our system, we did see a "burst", but notably it is a triggered burst, then a burst occurs. This is actually beneficial: it means no burst in unwanted location (stomach), but a quick release when needed (intestine). After the burst, the remaining release (from deeper pores) is slower and diffusion-controlled, which could continue to provide inhibitor over a longer period in the intestine (perhaps useful for sustained protease inhibition beyond the initial wave). A critical aspect for protein delivery is whether the protein remains functional after encapsulation and release. Trypsin inhibitor function was assessed by measuring how well the released STI could inhibit trypsin's enzymatic activity in solution. The trypsin activity assay results are summarized in Table 3, together with the corresponding sampling condition (SGF 2 h supernatant; SIF 4 h supernatant with or without Ca^{2+}) and the normalization used to define residual activity (blank trypsin control = 100%). Assay parameters (trypsin concentration, substrate concentration, buffer composition, and pre-incubation time) are as described in Methods to ensure the table is interpretable as a stand-alone dataset. Free trypsin (no inhibitor) had an initial activity defined as 100%. When an excess of free STI (molar STI:trypsin = 2:1) was added, the residual trypsin activity dropped to ~5%, essentially complete inhibition (the small remaining activity could be due to incomplete binding or experimental error). This establishes the maximum inhibition capacity of the STI we used. Trypsin mixed with the supernatant from PB-MSN after 2 h in SGF showed ~95% activity, meaning almost no inhibitor had been released into SGF – consistent with our direct release measurements (<5% release, which at the low concentration likely gave negligible inhibition). By contrast, trypsin mixed with the supernatant from PB-MSN after subsequent exposure to Ca^{2+} SIF (e.g. the 4 h SIF sample) showed only ~12% residual trypsin activity. In other words, the released STI in that sample was able to inhibit ~88% of trypsin activity. To rigorously quantify the functional preservation, we calculated the specific activity of the released protein compared to the native control.

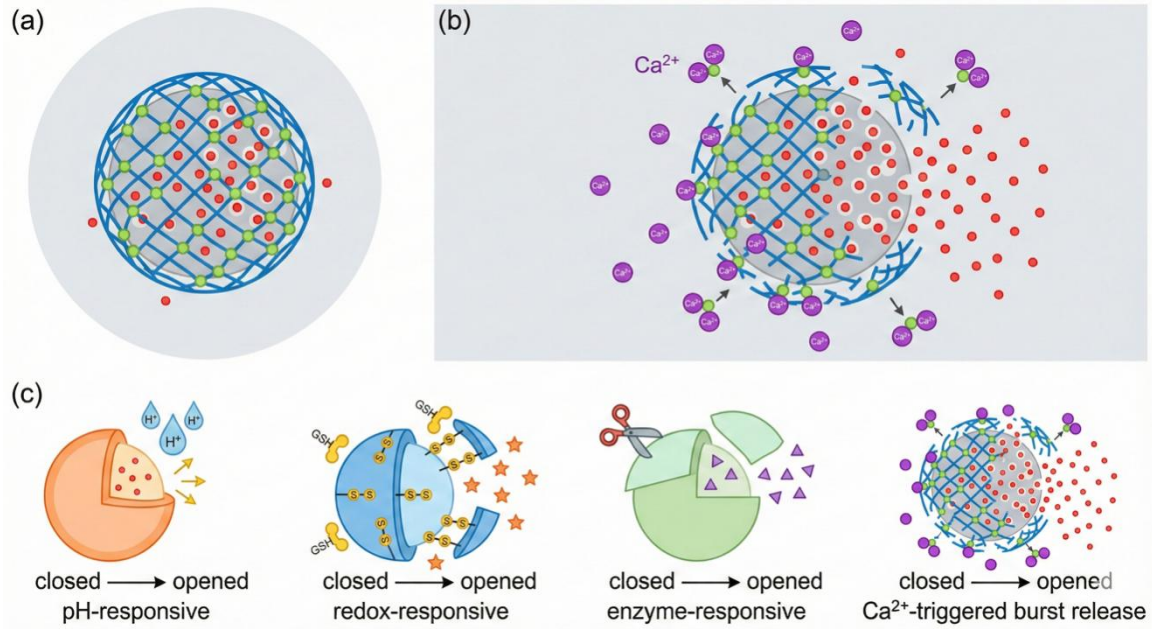

Figure 4. Schematic illustration of the Ca^{2+}-triggered disintegration of the borate-crosslinked PVA gate on STI-loaded PB-MSNs and the resulting release behavior. (a) The "closed" state: An MSN loaded with drug cargo is sealed by a polymer shell network (blue lines) stabilized by borate crosslinks. (b) The mechanism of Ca^{2+}-triggered release: Upon exposure to calcium ions (Ca^{2+}, purple spheres), competitive binding disrupts the borate crosslinks, causing the polymer shell to disassemble and triggering a rapid burst release of the cargo. (c) Conceptual comparison of different stimuli-responsive MSN systems, contrasting established pH-, redox-, and enzyme-responsive mechanisms with the Ca^{2+}-triggered burst release system depicted in (a) and (b)

10.57647/jnsc.2026.1603.11

Based on the assay definition where 1 TIU corresponds to 50% inhibition of trypsin activity, the native STI exhibited a specific activity of 2375 ± 45 TIU/mg. In comparison, the STI released from PB-MSNs following calcium triggering displayed a specific activity of 2200 ± 52 TIU/mg. This equates to a bioactivity retention of 92.6% relative to the native protein. This quantitative analysis confirms that the inhibitor's activity is largely preserved through the loading and release process, with only minimal loss likely attributable to minor denaturation during the acidic phase or interaction with the silica surface. These specific activity values demonstrate that the PB-MSN platform effectively safeguards the tertiary structure required for enzyme binding. As an additional check, we measured trypsin activity in presence of the particles themselves (to rule out adsorption of enzyme on particles affecting activity). We found that blank MSNs or coated MSNs without STI did not significantly inhibit trypsin (<5% change in activity), confirming that the inhibition observed is due to released STI, not any nonspecific effect of the carrier.A critical aspect for protein delivery is whether the protein remains functional after encapsulation and release. Trypsin inhibitor function was assessed by measuring how well the released STI could inhibit trypsin's enzymatic activity in solution. The trypsin activity assay results are summarized in Table 3, together with the corresponding sampling condition (SGF 2 h supernatant; SIF 4 h supernatant with or without Ca^{2+}) and the normalization used to define residual activity (blank trypsin control = 100%).

Assay parameters (trypsin concentration, substrate concentration, buffer composition, and pre-incubation time) are as described in Methods to ensure the table is interpretable as a stand-alone dataset. Free trypsin (no inhibitor) had an initial activity defined as 100%. When an excess of free STI (molar STI:trypsin = 2:1) was added, the residual trypsin activity dropped to ~5%, essentially complete inhibition (the small remaining activity could be due to incomplete binding or experimental error). This establishes the maximum inhibition capacity of the STI we used. Trypsin mixed with the supernatant from PB-MSN after 2 h in SGF showed ~95% activity, meaning almost no inhibitor had been released into SGF – consistent with our direct release measurements (<5% release, which at the low concentration likely gave negligible inhibition). By contrast, trypsin mixed with the supernatant from PB-MSN after subsequent exposure to Ca^{2+} SIF (e.g. the 4 h SIF sample) showed only ~12% residual trypsin activity. In other words, the released STI in that sample was able to inhibit ~88% of trypsin activity.

To rigorously quantify the functional preservation, we calculated the specific activity of the released protein compared to the native control. Based on the assay definition where 1 TIU corresponds to 50% inhibition of trypsin activity, the native STI exhibited a specific activity of 2375 ± 45 TIU/mg. In comparison, the STI released from PB-MSNs following calcium triggering displayed a specific activity of 2200 ± 52 TIU/mg. This equates to a bioactivity retention of 92.6% relative to the native protein.

This quantitative analysis confirms that the inhibitor's activity is largely preserved through the loading and release process, with only minimal loss likely attributable to minor denaturation during the acidic phase or interaction with the silica surface. These specific activity values demonstrate that the PB-MSN platform effectively safeguards the tertiary structure required for enzyme binding. As an additional check, we measured trypsin activity in presence of the particles themselves (to rule out adsorption of enzyme on particles affecting activity). We found that blank MSNs or coated MSNs without STI did not significantly inhibit trypsin (<5% change in activity), confirming that the inhibition observed is due to released STI, not any nonspecific effect of the carrier. These findings are significant because they demonstrate that encapsulation in MSNs and the PVA–borate coating process did not irreversibly inactivate the protein inhibitor.

The inhibitor molecules were effectively shielded in the MSN pores during the low pH phase (where otherwise trypsin inhibitor might have been chemically modified by acid hydrolysis or precipitated). Once released at neutral pH, they retain their tertiary structure needed to bind trypsin. This shows the promise of our approach not only for delivering protease inhibitors but potentially other delicate proteins.

The MSN protects them from denaturation in the stomach, and the sudden release in intestine yields an active payload. In sum, the release experiments confirm that our calcium-triggered system performs as designed: negligible release in the absence of trigger and rapid release upon Ca^{2+} triggering. The GI-simulated test demonstrated that the particles could survive a stomach-mimicking environment with minimal payload loss, then rapidly deploy the inhibitor in an intestinal setting when Ca^{2+} is present. This on/off behavior is desirable for intestinal-stage deployment under GI-mimicking in vitro conditions, because it demonstrates that cargo retention can be maintained in an acidic phase while rapid release can be triggered at near-neutral pH by Ca^{2+}.

However, these data should be interpreted as proof-of-concept for triggerable pore gating, not as a demonstration of in vivo oral-delivery efficacy, since gastric/intestinal fluids in vivo exhibit dynamic composition, complexation effects, and transport phenomena that are not captured in a simplified buffer-based protocol.These findings are significant because they demonstrate that encapsulation in MSNs and the PVA–borate coating process did not irreversibly inactivate the protein inhibitor.

10.57647/jnsc.2026.1603.11

Table 3. Trypsin activity assay for free STI and STI released from PB-MSNs under simulated gastrointestinal conditions (mean ± SD, n = 3). Specific activity is calculated based on 1 TIU = 50% inhibition

Sample tested (supernatant/timepoint where applicable)	Trypsin residual activity (%)	Inhibition (%)	Specific Activity (TIU/mg)
Free trypsin (no inhibitor; blank control)	100 ± 2	0	N/A
Free STI (positive control)	5 ± 1	95	2375 ± 45
PB-MSN SGF supernatant (2 h; pH 1.2 stage)	96 ± 3	4	Negligible
PB-MSN SIF (+Ca^{2+}) supernatant (4 h; pH 7.4 + 10 mM $CaCl_2$ stage)	12 ± 2	88	2200 ± 52
PB-MSN SIF (−Ca^{2+}) supernatant (4 h; pH 7.4 stage)	85 ± 5	15	Not calculated (low release)
Blank PB-MSN particles + trypsin (no STI)	98 ± 2	2	N/A

The inhibitor molecules were effectively shielded in the MSN pores during the low pH phase (where otherwise trypsin inhibitor might have been chemically modified by acid hydrolysis or precipitated). Once released at neutral pH, they retain their tertiary structure needed to bind trypsin. This shows the promise of our approach not only for delivering protease inhibitors but potentially other delicate proteins.

The MSN protects them from denaturation in the stomach, and the sudden release in intestine yields an active payload. In sum, the release experiments confirm that our calcium-triggered system performs as designed: negligible release in the absence of trigger and rapid release upon Ca^{2+} triggering. The GI-simulated test demonstrated that the particles could survive a stomach-mimicking environment with minimal payload loss, then rapidly deploy the inhibitor in an intestinal setting when Ca^{2+} is present. This on/off behavior is desirable for intestinal-stage deployment under GI-mimicking in vitro conditions, because it demonstrates that cargo retention can be maintained in an acidic phase while rapid release can be triggered at near-neutral pH by Ca^{2+}. However, these data should be interpreted as proof-of-concept for triggerable pore gating, not as a demonstration of in vivo oral-delivery efficacy, since gastric/intestinal fluids in vivo exhibit dynamic composition, complexation effects, and transport phenomena that are not captured in a simplified buffer-based protocol.

Importantly, the trypsin inhibition assay used here is intended to verify retention of inhibitory function after encapsulation and release under controlled conditions; it does not replicate the full intestinal digestion milieu, where multiple pancreatic enzymes (e.g., trypsin, chymotrypsin, elastase, carboxypeptidases), bile components, ionic speciation, and dynamic pH/transport processes jointly determine proteolysis and bioactivity. Standardized physiologically oriented in vitro digestion frameworks, such as the INFOGEST static protocol and its updates, explicitly incorporate multi-enzyme and bile phases and are therefore better suited for future evaluation of functional persistence and digestion-coupled performance.Importantly, the trypsin inhibition assay used here is intended to verify retention of inhibitory function after encapsulation and release under controlled conditions; it does not replicate the full intestinal digestion milieu, where multiple pancreatic enzymes (e.g., trypsin, chymotrypsin, elastase, carboxypeptidases), bile components, ionic speciation, and dynamic pH/transport processes jointly determine proteolysis and bioactivity. Standardized physiologically oriented in vitro digestion frameworks, such as the INFOGEST static protocol and its updates, explicitly incorporate multi-enzyme and bile phases and are therefore better suited for future evaluation of functional persistence and digestion-coupled performance.

From a safety and biocompatibility perspective, the materials used are benign. Silica is generally recognized as safe for oral use in pharmaceutical excipients (fumed silica is used in tablets, etc.), and mesoporous silica has shown good biocompatibility in numerous studies [68]. The PVA polymer is food-grade and non-toxic, and borate at the small amounts used would likely be chelated by dietary components or converted to boron micronutrients. Importantly, our system releases mostly calcium (a beneficial mineral) and borate (in trace amounts) upon activation. In future in vivo studies, one would need to consider the fate of the silica particles after release; likely they would be excreted or dissolved slowly. One advantage of using Ca^{2+} as trigger is that any residual silica could potentially further dissolve if doped with Ca (though we did not rely on doping here). We did briefly investigate whether incorporating Ca^{2+} into the silica framework (as per Liu et al. [22]) could be beneficial, but found that Ca-doped MSNs tend to release in acid (due to acid-labile Ca–O–Si bonds) which is the opposite of our goal. Thus, we chose the inert framework + external trigger approach.

Finally, beyond the specific application of trypsin inhibitor delivery, our calcium-triggered gating concept can be generalized. For example, other borate-binding polymers (like guar gum or alginate with cis-diols) could be used to gate MSNs for calcium-responsive behavior.

10.57647/jnsc.2026.1603.11

Table 4. Comparative summary of the Ca^{2+}-triggered PB-MSN system developed in this work and representative stimuli-responsive mesoporous silica nanoparticle delivery platforms reported in the literature

System / carrier	Stimulus	Gate / responsive element	Typical trigger condition (medium, pH, stimulus level)	Key release characteristics*	Representative reference(s)
pH-responsive STI-loaded MSNs from rice husk ash	pH (alkaline)	Surface-modified MSNs with pH-dependent electrostatic interactions	SIF-like buffer, pH 7–9 (no added Ca^{2+})	~15% STI released at pH 8 after 4 h; ~50% at pH 9 after 4 h; gradual pH-dependent desorption; no sharp on/off behavior.	[4]
PEG-coated MSNs for sustained macromolecule release	None (diffusion / time)	Dense PEG polymer "brush" capping	Physiological buffer, pH ~7.4 (no external stimulus)	Initial burst <10%; near zero-order release over several weeks; good burst suppression but no external trigger control; model protein trypsin inhibitor as cargo.	[14]
Redox-responsive disulfide-capped MSNs	Redox (GSH)	Disulfide-linked PEG or polymer cap	pH 7.4 buffer containing 5–10 mM glutathione (intracellular mimicking conditions)	Slow release at low GSH; accelerated release in 10 mM GSH; typical cumulative release 60–80% over 12–24 h; intracellular GSH level acts as trigger.	[71]
Enzyme-responsive peptide- or azo-peptide-capped MSNs	Enzymes (e.g. reductase, esterase, bacterial enzymes)	Enzyme-cleavable organic cap (e.g. azopyridinium or peptide linker)	Neutral buffer containing target enzyme or colon-mimicking enzymatic conditions	Minimal release without enzyme; enzyme presence gradually increases release (often 50–80% over 12–48 h); colon or intracellular enzyme expression defines trigger; in vitro studies show zero or very low leakage in the absence of target enzymes.	[72]
Ca-doped acid-degradable MSNs for tumor-microenvironment delivery	Acidic pH	Ca–O–Si bonds in silica framework (matrix degradation)	Acidic buffer (pH ~5.6) mimicking tumor or lysosomal environment versus pH 7.4 PBS	Low release at pH 7.4; accelerated matrix dissolution and drug release at pH 5–6; Ca^{2+} and drug co-released; Ca^{2+}-induced calcicoptosis and chemotherapy synergy reported for Ca-doped MSNs loaded with doxorubicin in tumor-mimicking conditions.	[22]
PB-MSN (this work): Ca^{2+}-triggered STI-loaded PVA–borate-gated MSNs	Ca^{2+} (ionic trigger)	PVA–borate nanogel gate at pore entrances	Stage 1: SGF, pH 1.2, no Ca^{2+}, 2 h; Stage 2: SIF, pH 7.4 + 10 mM $CaCl_2$, up to 8 h	<5% release in SGF (2 h); 3.8% ± 0.5% at 2 h SGF; rapid Ca^{2+}-triggered burst to ~40% within 0.5 h in SIF; 78% ± 3% at 4 h and 88–90% at 8 h with Ca^{2+}; ≤12% release in pH 7.4 SIF without Ca^{2+}; sharp on/off behavior and preserved STI activity (~88% trypsin inhibition).	[73]

Or alternative chemistries such as phosphate-crosslinked networks that dissolve upon encountering Ca^{2+} (since $Ca_3(PO_4)_2$ might precipitate, though that typically locks drug, but creative approaches might invert

10.57647/jnsc.2026.1603.11

it). Our success with PVA–borate suggests that using reversible crosslinkers that can be "broken" by a harmless trigger ion is a viable strategy. This might open avenues for designing oral delivery systems that respond to dietary cues or orally co-administered activators. Finally, beyond the specific application of trypsin inhibitor delivery, our calcium-triggered gating concept can be generalized. For example, other borate-binding polymers (like guar gum or alginate with cis-diols) could be used to gate MSNs for calcium-responsive behavior.

Table 4 provides a qualitative comparison of our system with other controlled release MSN systems, highlighting the stimulus, release control, and relevant data. In particular, compared to pH-only systems [69], the calcium-trigger offers a sharper on/off release (since pH-triggered often has gradual release between pH 7–8, whereas here the threshold behavior is more pronounced). Additionally, many enzyme-triggered systems (for colon-specific release, etc.) require the presence of specific bacterial enzymes – our system would not be limited by individual microbiome differences since Ca^{2+} is a ubiquitous trigger. A potential application of our calcium-triggered trypsin inhibitor delivery could be in treating conditions like pancreatitis or post-pancreatectomy syndromes, where temporary inhibition of trypsin in the gut is desired. An oral formulation could release the inhibitor precisely when pancreatic secretions (rich in Ca^{2+}) enter the intestine, thus modulating the digestive process in a controlled way. Another application is co-delivery with oral peptide drugs: for instance, one could co-encapsulate insulin and a protease inhibitor in separate compartments of a pill – the inhibitor could be in a Ca-triggered MSN like ours, while insulin maybe in an enteric-coated vehicle. Upon entering the intestine, Ca^{2+} triggers inhibitor release to shut down proteases, while insulin is then absorbed with less enzymatic degradation. This kind of combination therapy is indeed suggested by some oral delivery research [70]. Beyond safety, we clarify here how the present Ca^{2+}-triggered pore-gating concept could be extended to other therapeutic peptides/proteins. The mechanistic requirement is not specific to STI, but rather to (i) a cargo that can be stably loaded into the mesopores and (ii) a gate chemistry that remains intact under gastric-like conditions and undergoes rapid permeability increase or disassembly upon exposure to a defined Ca^{2+} stimulus at near-neutral pH. This logic is compatible with a wide range of peptide therapeutics and selected protein drugs for which oral delivery remains challenging due to proteolysis and low epithelial permeability. Clinically, the value proposition is underscored by the emergence of oral peptide products and technologies (e.g., oral semaglutide tablets as an orally administered GLP-1 receptor agonist, and oral octreotide capsules for acromegaly), despite the well-known constraints of GI degradation and absorption. Even where absolute bioavailability is low, orally dosed peptides such as desmopressin have long been viable in appropriate indications, emphasizing that enabling oral administration can be clinically meaningful when dosing and therapeutic window permit. We also explicitly note biological barriers that are not captured in the current buffer-based protocol.

First, intestinal mucus can trap or slow nanoparticles depending on surface chemistry, and mucus penetration versus mucoadhesion is a key determinant of access to the epithelium for orally administered nanocarriers. Consistent with this, our hydrophilic polymer shell is expected to modulate mucus interaction, but the net effect (muco-inert transport versus adhesion) must be measured in physiologically relevant mucus models.

Second, intestinal transit imposes a finite residence time window for trigger exposure, gate opening, and absorption; therefore, future optimization should consider (a) trigger thresholds under realistic ionic speciation, (b) the kinetics of gate disassembly in complex luminal media, and (c) whether a multipart dosage form that co-delivers Ca^{2+} can ensure timely activation within small-intestinal transit constraints. In future work, we will quantify cytocompatibility using standardized cell-viability assays and epithelial-relevant models (e.g., intestinal cell lines and/or co-culture mucus models), alongside complementary hemocompatibility and inflammatory readouts, to confirm the safety margin of the gated MSNs under conditions relevant to oral administration.

4. Conclusion

In this work we designed and validated a Ca^{2+}-triggered MSN delivery platform that combines gastric protection with on-demand intestinal release of a model macromolecular cargo, soybean trypsin inhibitor. Pore-expanded MSNs (~300 nm, pore diameter ~3.8 nm, BET surface area ~800 m_2/g) enabled high STI loading of 15.6 wt% (encapsulation efficiency 75%), and 14.5 wt% STI remained in the PB-MSN after deposition of an ~8 wt% PVA–borate gate without detectable drug loss.

Structural, textural and dispersion analyses confirmed that the mesoporous framework was preserved after coating while pore entrances were partially occluded. In SGF (pH 1.2, 2 h, no Ca^{2+}), PB-MSNs released only 3.8 ± 0.5% of STI versus 68 ± 5% from uncoated MSNs, demonstrating efficient suppression of gastric leakage. Upon transfer to SIF containing 10 mM $CaCl_2$, cumulative release from PB-MSNs rose to ~40% within 0.5 h, 78 ± 3% at 4 h and 88–90% at 8 h, whereas in Ca^{2+}-free SIF it remained ≤12.3 ± 1.5%, evidencing a sharp Ca^{2+}-dependent on/off behavior and competitive advantage over pH-only systems that typically require pH ≥ 9 to reach 50% STI release. Enzymatic assays showed that STI released under Ca^{2+} trigger preserved ~88% inhibition

10.57647/jnsc.2026.1603.11

of trypsin activity, comparable to free STI, while SGF supernatants showed negligible inhibition, confirming functional protection during gastric transit. Overall, these results establish borate-crosslinked PVA as an effective sacrificial gate for Ca^{2+}-mediated MSN disassembly and highlight Ca^{2+} as a benign, tunable trigger for spatiotemporally controlled protein delivery in GI-mimicking environments and, more broadly, for ion-responsive nanocarrier designs.

Importantly, this advance lies in adapting a well-known dynamic borate crosslinking principle to nanoscale pore gating on an inorganic mesoporous carrier, enabling an inverse trigger profile (stable in acid/low Ca^{2+}, activated in near-neutral/high Ca^{2+}) rather than introducing calcium- or borate-responsiveness as a general concept. Future work will focus on tuning crosslink density and Ca^{2+} threshold, integrating co-delivery of protease inhibitors with therapeutic peptides, and validating oral bioavailability enhancement and safety in relevant in vivo models. The modular nature of this platform should also enable adaptation to other protein cargos and clinically relevant ionic stimuli.

Author Contributions

Y.Q. and Y.X. conceived and designed the study. Y.Q., W.Z., and B.Z. carried out the experiments and collected the data. G.L. and Y.M. contributed to materials preparation and characterization. Q.Z. and X.W. performed data analysis and visualization. Y.Q. drafted the original manuscript. Y.X. supervised the project and critically revised the manuscript. All authors reviewed and approved the final version of the manuscript.

Availability of Data and Materials

The data supporting the findings of this study are available from the corresponding author upon reasonable request.

Conflict of Interest

The authors declare that they have no known competing financial interests or personal relationships that could have appeared to influence the work reported in this paper.

Ethical Approval

This study does not involve human participants or living organisms, and no ethical approval was required.

References

[1] Dang, Y., Guan, J. Nanoparticle-based drug delivery systems for cancer therapy. Smart Mater. *Med.* **1**, 10–19 (2020).

[2] Gao, Y., Gao, D., Shen, J., Wang, Q. A review of mesoporous silica nanoparticle delivery systems in chemo-based combination cancer therapies. Front. *Chem.* **8**, 598722 (2020).

[3] Lou, J., Best, M. D. Calcium-responsive liposomes: toward ion-mediated targeted drug delivery. *Methods Enzymol*. **640**, 105–129 (2020).

[4] Carneiro, A. A. B., Patekar, S., Goyal, M., De Campos, S. B., Bally, J., Hassanpour, M., Zhang, Z. pH-responsive mesoporous silica nanoparticles from rice husk ash for delivering trypsin inhibitor to control cotton bollworm. Ind. *Crops Prod*. **228**, 120934 (2025).

[5] Nicze, M., Borówka, M., Dec, A., Niemiec, A., Bułdak, Ł., Okopień, B. The current and promising oral delivery methods for protein- and peptide-based drugs. *Int. J. Mol. Sci*. **25**, 815 (2024).

[6] Jain, D., Mahammad, S. S., Singh, P. P., Kodipyaka, R. A. A review on parenteral delivery of peptides and proteins. Drug Dev. *Ind. Pharm*. **45**, 1403–1420 (2019).

[7] Onoue, S., Yamada, K., Sato, H. Advanced oral drug delivery systems: current challenges and emerging technologies. Acta Pharm. Sin. B (2025).

[8] Deraison, C., Vergnolle, N. Proteases in intestinal health and disease. Nat. Rev. Gastroenterol. *Hepatol*. **22**, 1–23 (2025).

[9] Islam, M. R., Ihenacho, K., Park, J. W., Islam, I. S. Plasmid DNA nicking: a novel activity of soybean trypsin inhibitor and bovine aprotinin. *Sci. Rep.* **9**, 11596 (2019).

[10] Kunitz, M. Crystalline soybean trypsin inhibitor. *J. Gen. Physiol*. **30**, 291–310 (1947).

[11] Coria, L. M., Pueblas Castro, C., Bruno, L., Nakaya, H. I., Pasquevich, K. A., Cassataro, J. Discovery of protease inhibitors from bacteria as novel adjuvants for oral vaccine formulations. *Front. Immunol.* **16**, 1679540 (2025).

[12] Sharma, V., Devkota, L., Kishore, N., Dhital, S. Understanding the interplay between dietary fiber, polyphenols, and digestive enzymes. *Food Hydrocoll*. **166**, 111310 (2025).

[13] de Souza Nascimento, A. M., de Oliveira Segundo, V. H., Felipe Camelo Aguiar, A. J., Piuvezam, G., Souza Passos, T., Florentino da Silva Chaves Damasceno, K. S. F. S., de Araújo Morais, A. H. Antibacterial action mechanisms and mode of trypsin inhibitors: a systematic review. *J. Enzyme Inhib. Med. Chem*. **37**, 749–759 (2022).

[14] Bhattacharyya, S., Wang, H., Ducheyne, P. Polymer-coated mesoporous silica nanoparticles for the controlled release of macromolecules. *Acta Biomater*. **8**, 3429–3435 (2012).

[15] Carneiro, A. A. B., Patekar, S., Goyal, M., de Almeida, S., Dayarathne, N. K., De Campos, S. B., Bally, J.,

Hassanpour, M., Zhang, Z. Lignin-enabled silica hybrid nanoparticles from rice husk for improved biopesticide delivery and cotton bollworm control. *Int. J. Biol. Macromol.* **309**, 142589 (2025).

[16] Pikor, D., Hurła, M., Słowikowski, B., Szymanowicz, O., Poszwa, J., Banaszek, N., Drelichowska, A., Jagodziński, P. P., Kozubski, W., Dorszewska, J. Calcium ions in the physiology and pathology of the central nervous system. *Int. J. Mol. Sci*. **25**, 13133 (2024).

[17] Luan, S., Wang, C. Calcium signaling mechanisms across kingdoms. *Annu. Rev. Cell Dev. Biol*. **37**, 311–340 (2021).

[18] Klipp, A., Greitens, C., Scherer, D., Elsener, A., Leroux, J.-C., Burger, M. Modular calcium-responsive and CD9-targeted phospholipase system enhancing endosomal escape for DNA delivery. *Adv. Sci.* **12**, 2410815 (2025).

[19] Hunt, H., Tilūnaitė, A., Bass, G., Soeller, C., Roderick, H. L., Rajagopal, V., Crampin, E. J. Ca2+ release via IP3 receptors shapes the cardiac Ca2+ transient for hypertrophic signaling. *Biophys. J.* **119**, 1178–1192 (2020).

[20] Liu, C., Tang, X., Huang, G. Biodegradable Ca2+ doped mesoporous silica nanoparticles promote chemotherapy synergism with calcicoptosis and activate anti-tumor immunity. *Inorganics* **12**, 152 (2024).

[21] Choi, E., Lim, D.-K., Kim, S. Calcium-doped mesoporous silica nanoparticles as a lysosomolytic nanocarrier for amine-free loading and cytosolic delivery of siRNA. *J. Ind. Eng. Chem*. 81, 71–80 (2020).

[22] Dan, N., Samanta, K., Almoazen, H. An update on pharmaceutical strategies for oral delivery of therapeutic peptides and proteins in adults and pediatrics. *Children* **7**, 307 (2020).

[23] Xu, B., Li, S., Shi, R., Liu, H. Multifunctional mesoporous silica nanoparticles for biomedical applications. *Sig. Transduct. Target. Ther*. **8**, 435 (2023).

[24] Zhu, H., Zeng, J., Jiang, S., Huang, S., Xie, Z., Huang, Y., Lin, S., Wang, B. Poly(vinyl alcohol)/borax/modified silver nanowire composite hydrogel with self-healing, high conductivity, and electromagnetic interference shielding properties. *J. Alloys Compd.* **1011**, 178437 (2025).

[25] Wu, H., Su, Q., Zhou, R., Yan, J., Feng, Y., Guan, C., Su, W., Chen, D., Tang, L., Huang, X., et al. Synergistic borate crosslinking and chain entanglement for mechanically robust and water-rich hydrogels. *J. Colloid Interface Sci*. **702**, 138972 (2026).

[26] Taniguchi, T., Urayama, K. Linear dynamic viscoelasticity of dual cross-link poly(vinyl alcohol) hydrogel with determined borate ion concentration. *Gels* **7**, 71 (2021).

[27] Lou, J., Carr, A. J., Watson, A. J., Mattern-Schain, S. I., Best, M. D. Calcium-responsive liposomes via a synthetic lipid switch. *Chem. Eur. J.* **24**, 3599–3607 (2018).

[28] Rogers, H. R., van den Berg, C. M. G. Determination of borate ion-pair stability constants by potentiometry and non-approximative linearization of titration data. *Talanta* **35**, 271–275 (1988).

[29] Hu, C., Lu, W., Mata, A., Nishinari, K., Fang, Y. Ions-induced gelation of alginate: mechanisms and applications. *Int. J. Biol. Macromol*. **177**, 578–588 (2021).

[30] Mao, J., Liu, B., Xiao, Y., Yang, X., Lin, C., Zhang, Y., Wang, Q., Zhang, Q. Study of crosslinker size on the rheological properties of borate crosslinked guar gum. *Int. J. Biol. Macromol*. **231**, 123284 (2023).

[31] Chen, J., Xu, Z., Zhang, M., Ju, Z., Niu, Z., Ma, Y., Xu, Z., Zhang, T., Shi, F. Mesoporous silica nanoparticles: a synthesis guide and research progress in the biomedical field. Mater. *Today Chem*. **42**, 102426 (2024).

[32] Carvalho, G. C., Marena, G. D., Karnopp, J. C. F., Jorge, J., Sábio, R. M., Martines, M. A. U., Bauab, T. M., Chorilli, M. Cetyltrimethylammonium bromide in the synthesis of mesoporous silica nanoparticles: general aspects and in vitro toxicity. *Adv. Colloid Interface Sci.* **307**, 102746 (2022).

[33] Martinez-Ortigosa, J., Millán, R., Simancas, J., Hernández-Rodríguez, M., Vidal-Moya, J. A., Jordá, J. L., Martineau-Corcos, C., Sarou-Kanian, V., Boronat, M., Blasco, T., et al. Crystalline phase transition in as-synthesized pure silica zeolite RTH containing tetra-alkyl phosphonium as organic structure directing agent. *J. Mater. Chem. A* **12**, 876–891 (2024).

[34] Li, X., Yin, H., Zhang, J., Liu, J., Chen, G. Effect of organic template removal approaches on physiochemical characterization of Ni/Al-SBA-15 and eugenol hydrodeoxygenation. *J. Solid State Chem*. **282**, 121063 (2020).

[35] Kong, X., Li, Y., Liu, X. Purification of soybean Kunitz trypsin inhibitor and the mechanism of its passivation by lysine and disulfide bond modifications. *Food Biosci*. 55, 103042 (2023).

[36] Wang, A., Ma, Y., Zhao, D. Pore engineering of porous materials: effects and applications. *ACS Nano* **18**, 22829–22854 (2024).

[37] Kong, J., Park, S. S., Ha, C.-S. pH-sensitive polyacrylic acid-gated mesoporous silica nanocarrier incorporated with calcium ions for controlled drug release. *Materials* **15**, 5926 (2022).

[38] Wang, Y., Zhao, K., Xie, L., Li, K., Zhang, W., Xi, Z., Wang, X., Xia, M., Xu, L. Construction of calcium carbonate-liposome dual-film coated mesoporous silica as a delayed drug release system for antitumor therapy. *Colloids Surf. B Biointerfaces* **212**, 112357 (2022).

[39] da Silva, J. A. L. Borate esters of polyols: occurrence, applications and implications. *Inorg. Chim. Acta* **520**, 120307 (2021).

[40] Ireland, P., Fordtran, J. S. Effect of dietary calcium and age on jejunal calcium absorption in humans studied by intestinal perfusion. *J. Clin. Invest.* **52**, 2672–2681 (1973).

[41] MacConaill, M. Calcium precipitation from mammalian physiological salines (Ringer solutions) and the preparation of high [Ca] media. *J. Pharmacol. Methods* **14**, 147–155 (1985).

[42] Wang, J., Zhao, M., Liu, T., Feng, F., Zhou, A. Guidelines for the digestive enzymes inhibition assay. eFood 3, e31 (2022).

[43] Polyakov, Y. S., Zydney, A. L. Ultrafiltration membrane performance: effects of pore blockage/constriction. *J. Membr. Sci.* **434**, 106–120 (2013).

[44] Galata, D. L., Péterfi, O., Ficzere, M., Szabó-Szőcs, B., Szabó, E., Nagy, Z. K. The current state-of-the art in pharmaceutical continuous film coating: a review. *Int. J. Pharm.* **669**, 125052 (2025).

[45] Palomeque Chávez, J. C., Mohammed, A. A., Aghajanpour, S., Li, S., Enzo, S., Kelly, N. L., Bradley, D. G., Kerherve, G., Porter, A. E., Hanna, J. V., et al. One-pot sol–gel synthesis of Sr/Ca-doped silica nanoparticles for osteogenic therapy in osteoporosis. *Front. Nanotechnol***.** **7**, 1634210 (2025).

[46] Jurašin, D. D., Ćurlin, M., Capjak, I., Crnković, T., Lovrić, M., Babič, M., Horák, D., Vrček, I. V., Gajović, S. Surface coating affects behavior of metallic nanoparticles in a biological environment. *Beilstein J. Nanotechnol*. **7**, 246–262 (2016).

[47] Trayford, C., van Rijt, S. In situ modified mesoporous silica nanoparticles: synthesis, properties and theranostic applications. *Biomater. Sci.* **12**, 5450–5467 (2024).

[48] Xie, X., Yang, D. Self-healing thermally conductive polymer composites based on polyvinyl alcohol with dynamic borate ester and hydrogen bonds. Compos. *Part A Appl. Sci. Manuf.* **181**, 108131 (2024).

[49] Fitzsimons, B., Parry, T. Coating failures and defects. In Protective Organic Coatings; Tator, K. B., Ed.; ASM International, 502–512 (2015).

[50] Krebs, J., Agellon, L. B., Michalak, M. Ca2+ homeostasis and endoplasmic reticulum (ER) stress: an integrated view of calcium signaling. *Biochem. Biophys. Res. Commun*. **460**, 114–121 (2015).

[51] Ye, J., Liu, L., Lan, W., Xiong, J. Targeted release of soybean peptide from CMC/PVA hydrogels in simulated intestinal fluid and their pharmacokinetics. *Carbohydr. Polym*. **310**, 120713 (2023).

[52] Chang, S.-H. A dishing model for STI CMP process. Microelectron. *Eng*. **82**, 136–142 (2005).

[53] Cui, M., Zhang, M., Liu, K. Colon-targeted drug delivery of polysaccharide-based nanocarriers for synergistic treatment of inflammatory bowel disease: a review. Carbohydr. *Polym*. **272**, 118530 (2021).

[54] Khalbas, A. H., Albayati, T. M., Ali, N. S., Salih, I. K. Drug loading methods and kinetic release models using of mesoporous silica nanoparticles as a drug delivery system: a review. *S. Afr. J. Chem. Eng*. **50**, 261–280 (2024).

[55] Shalon, D., Culver, R. N., Grembi, J. A., Folz, J., Treit, P. V., Shi, H., Rosenberger, F. A., Dethlefsen, L., Meng, X., Yaffe, E., et al. Profiling the human intestinal environment under physiological conditions. *Nature* **617**, 581–591 (2023).

[56] Fatima, R., Katiyar, P., Kushwaha, K. Recent advances in mesoporous silica nanoparticle: synthesis, drug loading, release mechanisms, and diverse applications. *Front. Nanotechnol.* **7**, 1564188 (2025).

[57] Mace, O. J., Morgan, E. L., Affleck, J. A., Lister, N., Kellett, G. L. Calcium absorption by Cav1.3 induces terminal web myosin II phosphorylation and apical GLUT2 insertion in rat intestine. *J. Physiol*. **580**, 605–616 (2007).

[58] Niewiadomski, K., Szopa, D., Pstrowska, K., Wróbel, P., Witek-Krowiak, A. Comparative analysis of crosslinking methods and their impact on the physicochemical properties of SA/PVA hydrogels. *Materials* **17**, 1816 (2024).

[59] Al-Emam, E., Soenen, H., Caen, J., Janssens, K. Characterization of polyvinyl alcohol-borax/agarose (PVA-B/AG) double network hydrogel utilized for the cleaning of works of art. *Herit. Sci.* **8**, 106 (2020).

[60] Li, J., Liu, Y., Chen, Q. Conformation of dilute poly(vinyl alcohol)-borax complex by asymmetric flow field-flow fractionation. *J. Chromatogr. A* **1624**, 461260 (2020).

[61] Khalil, A. K. A., Teow, Y. H., Takriff, M. S., Ahmad, A. L., Atieh, M. A. Recent developments in stimuli-responsive polymer for emerging applications: a review.

Results Eng. **25**, 103900 (2025).

[62] Guo, P., Liang, J., Li, Y., Lu, X., Fu, H., Jing, H., Guan, S., Han, D., Niu, L. High-strength and pH-responsive self-healing polyvinyl alcohol/poly 6-acrylamidohexanoic acid hydrogel based on dual physically cross-linked network. Colloids Surf. *A Physicochem. Eng. Asp*. **571**, 64–71 (2019).

[63] Fu, S., Rempson, C. M., Puche, V., Zhao, B., Zhang, F. Construction of disulfide containing redox-responsive polymeric nanomedicine. *Methods* **199**, 67–79 (2022).

[64] Nakagawa, T., Wang, X., Miguez-Cabello, F. J., Bowie, D. The open gate of the AMPA receptor forms a Ca2+ binding site critical in regulating ion transport. *Nat. Struct. Mol. Biol*. **31**, 688–700 (2024).

[65] Nair, A., Chandrashekhar H., R., Day, C. M., Garg, S., Nayak, Y., Shenoy, P. A., Nayak, U. Y. Polymeric functionalization of mesoporous silica nanoparticles: biomedical insights. *Int. J. Pharm*. **660**, 124314 (2024).

[66] Lérida-Viso, A., Estepa-Fernández, A., García-Fernández, A., Martí-Centelles, V., Martínez-Máñez, R. Biosafety of mesoporous silica nanoparticles: towards clinical translation. *Adv. Drug Deliv. Rev*. **201**, 115049 (2023).

[67] Adepu, S., Ramakrishna, S. Controlled drug delivery systems: current status and future directions. *Molecules* **26**, 5905 (2021).

[68] Deluque, A. L., Dimke, H., Alexander, R. T. Biology of calcium homeostasis regulation in intestine and kidney. *Nephrol. Dial. Transplant*. **40**, 435–445 (2025).

[69] Cui, Y., Dong, H., Cai, X., Wang, D., Li, Y. Mesoporous silica nanoparticles capped with disulfide-linked PEG gatekeepers for glutathione-mediated controlled release. *ACS Appl. Mater. Interfaces* **4**, 3177–3183 (2012).

[70] Mas, N., Agostini, A., Mondragón, L., Bernardos, A., Sancenón, F., Marcos, M. D., Martínez-Máñez, R., Costero, A. M., Gil, S., Merino-Sanjuán, M., et al. Enzyme-responsive silica mesoporous supports capped with azopyridinium salts for controlled delivery applications. *Chem. Eur. J.* **19**, 1346–1356 (2013).

[71] Haq, I. U., Liu, H., Ghafar, M. A., Zafar, S., Subhan, M., Abbasi, A., Hyder, M., Basit, A., Rebouh, N. Y., Hou, Y. Mesoporous silica nanoparticles impair physiology and reproductive fitness of Tuta absoluta through plant-mediated oxidative stress and enzymatic disruption. *Insects* **16**, 877 (2025).

[72] Mahanur, V. B., Khandale, N. B., Tekade, M. S., Singh, S. K. Harnessing Lipid based nanocochleates for targeted therapeutic delivery: Addressing formulation bottlenecks and advancements. Colloids and surfaces B: Biointerfaces 258, 115287 (2026).

[73] Lee, J. M., Kang, S. J., Yoon, M. S., Jo, M. J., Yoo, M. K., Park, S. Y., Bong, S., Kim, J., Park, S., Lee, Y., Shin, Y., Lee, H. J., Kim, J. S., Park, C. W., Shin, D. H. Recent advances in nanosacle sprayable hydrogels for cancer managemnet: Nanoparticle-loaded formulations for therapy and prevention. International Jpurnal of Nanomedicine 21, 1-39 (2026).

Apendix

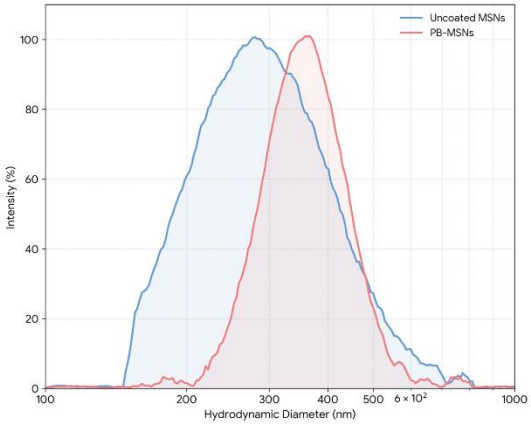

Figure S1. Hydrodynamic size distributions measured by Dynamic Light Scattering (DLS) for Uncoated MSNs and PVA–borate coated MSNs (PB-MSNs) in aqueous dispersion. The uncoated MSNs (blue curve) exhibit a broader distribution indicating a tendency toward slight aggregation, while the PB-MSNs (red curve) display a narrower, unimodal peak shifted to a larger hydrodynamic diameter due to the presence of the hydrated polymer coating and improved colloidal stability

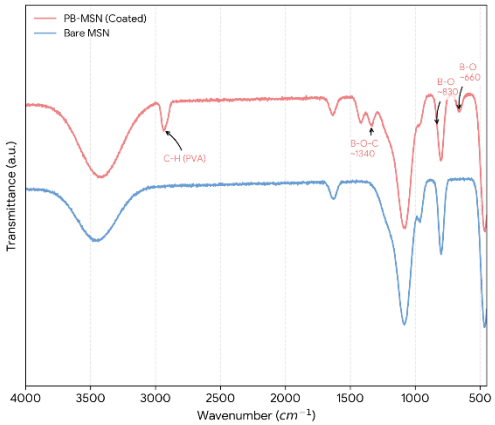

Figure S2. ATR-FTIR spectra of uncoated MSNs and PVA–borate–gated MSNs (PB-MSN)

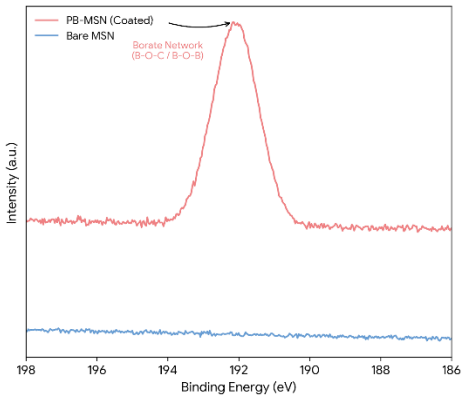

Figure S3. High-resolution spectra highlight the appearance of a B 1s signal in PB-MSN attributable to borate-derived B–O environments; peak positions/assignments are consistent with literature-reported B–O–B and B–O–C components in the ~191.8–192.4 eV range, supporting successful PVA–borate gating

10.57647/jnsc.2026.1603.11

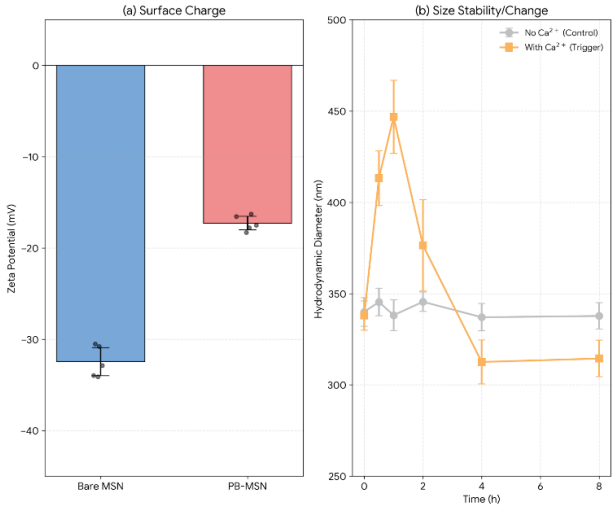

Figure S4. Expanded colloidal analysis of the nanoparticle formulations. (a) Zeta potential measurements of bare MSN and PB-MSN, confirming surface modification by the PVA–borate coating. (b) Time-dependent hydrodynamic diameter (DLS) tracking of PB-MSN in pH 7.4 buffer in the absence (control) and presence of 10 mM Ca^{2+}, demonstrating the calcium-triggered swelling and disintegration of the coating

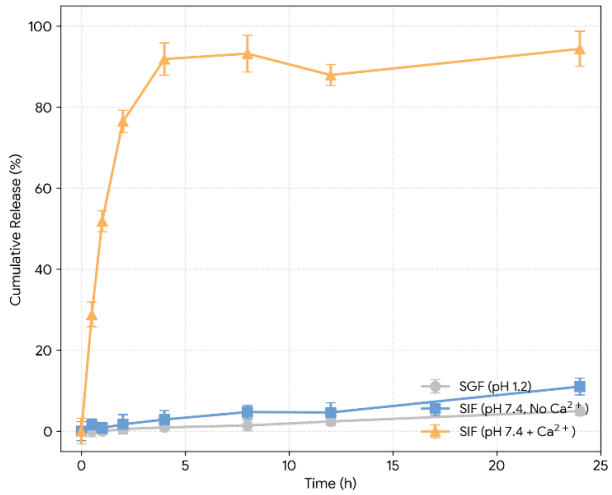

Figure S5. Coating stability/disintegration behavior of PB-MSN under simulated gastric and intestinal media. The PVA–borate gate remains stable in Ca^{2+}-free SGF and Ca^{2+}-free SIF, whereas inclusion of Ca^{2+} produces rapid structural change consistent with Ca^{2+}-mediated disruption of borate–diol crosslinks and accelerated network dissolution/permeabilization

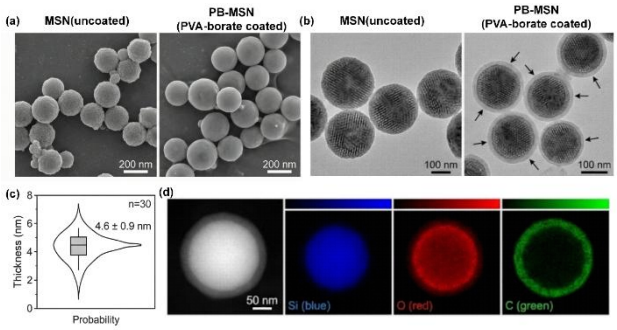

Figure S6. Representative (a) SEM images and (b) TEM micrographs of uncoated MSNs and PB-MSNs showing preservation of particle morphology after coating and the appearance of a thin peripheral layer on PB-MSNs. (c) Quantification of coating thickness extracted from TEM images by measuring the shell layer at multiple positions across multiple particles ($n \geq 30$). (d) HAADF-STEM image with corresponding elemental maps (Si and O for the silica framework and C for the polymer-enriched exterior region)

10.57647/jnsc.2026.1603.11

Table S1. Mass balance of STI during two-stage simulated GI release from PB-MSNs (mean ± SD, n = 3)

Two-stage condition	Initial STI loaded (mg)	Released in supernatant (mg, %)	Residual in particles (mg, %)	Unrecovered/adsorbed (mg, %)	Total recovery (%)
SGF 2 h → SIF 8 h (+10 mM $CaCl_2$)	7.25 ± 0.25	6.38 ± 0.36, 88.0 ± 4.0	0.72 ± 0.30, 10.0 ± 4.1	0.15 ± 0.05, 2.0 ± 0.7	100.0 ± 2.2
SGF 2 h → SIF 8 h ($-Ca^{2+}$)	7.25 ± 0.25	0.89 ± 0.12, 12.3 ± 1.5	6.21 ± 0.26, 85.7 ± 1.8	0.15 ± 0.05, 2.0 ± 0.7	100.0 ± 2.1

Table S2. DLS Characterization of Uncoated and PVA–Borate Coated MSNs across three independent batches

Sample Formulation	Batch	Z-Average Diameter (nm)	PDI
	1	318.5	0.345
Uncoated MSNs	2	326.2	0.362
	3	321.8	0.338
Mean ± SD		322.2 ± 3.9	0.348 ± 0.012
	1	368.4	0.185
PB-MSNs (Coated)	2	372.1	0.192
	3	369.7	0.178
Mean ± SD		370.1 ± 1.9	0.185 ± 0.007

10.57647/jnsc.2026.1603.11